Chemical abundances in Seyfert galaxies – X. Sulphur abundance estimates

Oli L. Dors [1]*, M. Valerdi [2]*, R. A. Riffel [3], R. Riffel [4], M. V. Cardaci [5,6], G. F. Hägele,[5,6]
Mark Armah [4], M. Revalski,[7] S. R. Flury [8], P. Freitas-Lemes,[1] E. B. Amôres,[9] A. C. Krabbe [1],
L. Binette,[10,11] A. Feltre [12] and T. Storchi-Bergmann[4]

[1] *Universidade do Vale do Paraíba, Av. Shishima Hifumi 2911, CEP 12244-000 São José dos Campos, SP, Brazil*
[2] *Instituto Nacional de Astrofísica, Óptica y Electrónica (INAOE), Luis E. Erro No. 1, Sta María Tonantzintla, C.P. 72840 Puebla, Mexico*
[3] *Departamento de Física, Centro de Ciências Naturais e Exatas, Universidade Federal de Santa Maria, 97105-900 Santa Maria, RS, Brazil*
[4] *Departamento de Astronomia, Universidade Federal do Rio Grande do Sul, Av. Bento Gonçalves 9500, Porto Alegre, CP 15051, 91501-970 RS, Brazil*
[5] *Facultad de Ciencias Astronómicas y Geofísicas, Universidad Nacional de La Plata, Paseo del Bosque s/n, 1900 La Plata, Argentina*
[6] *Instituto de Astrofísica de La Plata (CONICET-UNLP), Avenida Centenario (Paseo del Bosque) s/n, B1900FWA La Plata, Argentina*
[7] *Space Telescope Science Institute, 3700 San Martin Drive, Baltimore, MD 21218, USA*
[8] *Department of Astronomy, University of Massachusetts Amherst, Amherst, MA 01002, USA*
[9] *Departamento de Física, Universidade Estadual de Feira de Santana, Av. Transnordestina s/n, CEP 44036-900 Feira de Santana, BA, Brazil*
[10] *Instituto de Astronomía, Universidad Nacional Autónoma de México, A.P. 70-264, 04510 México, D.F., México, Mexico*
[11] *Département de physique, de génie physique et d'optique, Université Laval, Québec, QC G1V 0A6, Canada*
[12] *Osservatorio di Astrofisica e Scienza dello Spazio di Bologna, Via P. Gobetti 93/3, I-40129 Bologna, Italy*

ABSTRACT

For the first time, the sulphur abundance relative to hydrogen (S/H) in the narrow-line regions of a sample of Seyfert 2 nuclei (Sy 2s) has been derived via direct estimation of the electron temperature. Narrow emission-line intensities from the Sloan Digital Sky Survey (SDSS) Data Release 17 (DR17) [in the wavelength range $3000 < \lambda(\text{Å}) < 9100$] and from the literature for a sample of 45 nearby ($z < 0.08$) Sy 2s were considered. Our direct estimates indicate that Sy 2s have similar temperatures in the gas region where most of the S^+ ions are located in comparison with that of star-forming regions (SFs). However, Sy 2s present higher temperature values ($\sim 10\,000$ K) in the region where most of the S^{2+} ions are located relative to that of SFs. We derive the total sulphur abundance in the range of $6.2 \lesssim 12 + \log(\text{S/H}) \lesssim 7.5$, corresponding to 0.1–1.8 times the solar value. These sulphur abundance values are lower by ~ 0.4 dex than those derived in SFs with similar metallicity, indicating a distinct chemical enrichment of the interstellar medium (ISM) for these object classes. The sulphur abundance relative to oxygen (S/O) values for our Sy 2 sample present an abrupt (~ 0.5 dex) decrease with increasing oxygen abundance relative to hydrogen (O/H) for the high-metallicity regime [$12 + \log(\text{O/H}) \gtrsim 8.7$)], what is not seen for the SFs. However, when our Sy 2 estimates are combined with those from a large sample of SFs, we did not find any dependence between S/O and O/H.

Key words: ISM: abundances – galaxies: abundances – galaxies: active – galaxies: evolution – galaxies: nuclei – galaxies: Seyfert.

1 INTRODUCTION

Sulphur is mainly produced via α-capture in the inner layers of massive stars (e.g. Woosley & Weaver 1995; Nomoto, Kobayashi & Tominaga 2013) and it is a truly non-refractory element in the interstellar medium (ISM). Because of these features, the sulphur abundance and its abundance relation with the oxygen (S/O) place constraints on stellar nucleosynthesis calculations, variations of the initial mass function (IMF) of stars and in the analysis of the oxygen depletion on to dust grains (e.g. Garnett 1989; Savage & Sembach 1996; Henry, Kwitter & Balick 2004).

Over time, several studies have obtained sulphur (and other α-elements) and oxygen abundances in star-forming regions (H II

regions and H II galaxies, hereafter SFs; e.g. Pagel 1978; Shields & Searle 1978; Vilchez et al. 1988; Christensen, Petersen & Gammelgaard 1997; Garnett et al. 1997; Vermeij & van der Hulst 2002; Kennicutt, Bresolin & Garnett 2003; Pérez-Montero et al. 2006; Hägele et al. 2008; López-Sánchez & Esteban 2009; Berg et al. 2013, 2020; Dors et al. 2016; Fernández et al. 2019; Arellano-Córdova et al. 2020; Rogers et al. 2021). However, the S/O versus O/H relation is still ill-defined. In fact, some authors (e.g. Vilchez et al. 1988; Díaz et al. 1991; Dors et al. 2016; Díaz & Zamora 2022) have found evidence that S/O decreases as O/H increases. On the other hand, constant S/O abundance over a wide range of O/H (a gas phase metallicity tracer)[1] is supported by a growing body of studies (e.g.

[1] For a review see Maiolino & Mannucci (2019) and Kewley, Nicholls & Sutherland (2019).

* E-mail: olidors@univap.br (OLD); mvalerdi@astro.unam.mx (MV)

Garnett 1989; Kennicutt et al. 2003; Izotov et al. 2006; Guseva et al. 2011; Berg et al. 2020; Rogers et al. 2021).

Abundance estimates in stellar atmospheres, derived from absorption features, have confirmed the above contradictory results and several scenarios have been reported: (i) a constant increase of the S/Fe abundance ratio as metallicity[2] decreases (e.g. Israelian & Rebolo 2001; Takada-Hidai et al. 2002); (ii) an increase of S/Fe followed by a constant value at the metal-poor regime as metallicity decreases (Nissen et al. 2004, 2007); and (iii) a bimodal behaviour of S/Fe at the metal-poor regime (Caffau et al. 2005). However, recent chemical abundance determinations in stellar atmospheres have found a decrease of S/Fe with increasing Fe/H (Costa Silva, Delgado Mena & Tsantaki 2020; Lucertini et al. 2022). In additional, stellar abundance results from the AMBRE Project (Perdigon et al. 2021), which contain the largest sulfur estimates in Galactic stars, clearly found a decrease of S/Fe with increasing stellar metallicties (see also Recio-Blanco et al. 2022; Gaia Collaboration et al. 2022)**.** Interestingly, abundance estimates based on absorption lines in damped Lyα (DLA) systems (Centurión et al. 2000) showed a decrease of S/Zn with the increase of Zn/H (a metallicity tracer; Pettini et al. 1997), indicating that α-element burning happens at different times for different elements in massive stars (see also Bonifacio et al. 2001; Prochaska & Wolfe 2002; Fathivavsari et al. 2013; Fox, Richter & Fechner 2014). However, gas-phase abundances in DLAs must be corrected for dust depletion effects, producing additional difficulties in the interpretation of abundance ratio trends (e.g. Roman-Duval et al. 2022).

Sulphur and oxygen abundances have also been largely derived for planetary nebulae (PNe; e.g. Barker 1980; Aller & Czyzak 1983; Costa, Uchida & Maciel 2004; Bernard-Salas et al. 2008; Cavichia et al. 2017; Pagomenos, Bernard-Salas & Pottasch 2018; Walsh et al. 2018; Espíritu & Peimbert 2021; García-Rojas et al. 2022). In particular, Fang et al. (2018), who combined S and O abundances, obtained a clear decrease of S/O with O/H for 10 PNe in the Andromeda Galaxy (M31) with estimates relying on data from the literature. Additionally, these authors found that their sample of PNe have abundance estimates ∼0.2–0.4 dex lower than the expected sulphur-to-oxygen abundance solar value assuming $\log(S/O)_\odot = -1.43$ (Grevesse & Sauval 1998; Allende Prieto, Lambert & Asplund 2001). This discrepancy has previously been attributed to the inadequacy of the ionization correction factors (ICFs) used to correct the presence of unobserved sulphur ions (the so-called 'sulphur anomaly') by Henry et al. (2004) and Milingo et al. (2010). However, the PN abundance estimates by Fang et al. (2018) are in agreement with those derived in H II regions also located at the Andromeda Galaxy by Zurita & Bresolin (2012), confirming their results. Moreover, Delgado-Inglada, Morisset & Stasińska (2014), who computed a large grid of photoionization models that covers a wide range of physical parameters and is representative of most observed PNe, proposed a robust ICF for the sulphur and, by using optical observational data for a large sample, confirmed that S/O decreases with O/H. However, it is worth to mention that, contrary to presently accepted thinking, Jenkins (2009) showed that sulphur can deplete by up to ∼1 dex, which might account for some of the decrease observed.

Contrary to SFs, stars, DLA systems, and PNe, the sulphur abundance is poorly known in active galactic nuclei (AGNs) or only qualitative estimates are available in the literature. The first

(qualitative) sulphur estimates for this class of objects seem to have been performed by Storchi-Bergmann & Pastoriza (1990), who compared the intensity of the [N II]($\lambda\lambda$6548, 6584)/Hα and [S II]($\lambda\lambda$6716, 31)/Hα line ratios predicted by photoionization models with observational data from a sample of 177 Seyfert 2 galaxies. These authors found that models assuming sulphur abundances ranging from half to five times the solar abundance reproduce the observational data. These estimates can be somewhat uncertain because the model fittings by Storchi-Bergmann & Pastoriza (1990) do not consider the lines emitted by S^{2+}, which can be the most abundant sulphur ion and occurs as a result of high ionization degree of the AGNs (e.g. Richardson et al. 2014; Pérez-Díaz et al. 2021).

Recently, Dors et al. (2020b) proposed a new methodology for the T_e method – a conventional and reliable method (Pilyugin 2003; Toribio San Cipriano et al. 2017) based on direct estimates of the electron temperature (for a review see Peimbert, Peimbert & Delgado-Inglada 2017; Pérez-Montero 2017) – which makes it possible to estimate the O/H abundance in Seyfert 2 nuclei (hereafter Sy 2s). Further studies based on this methodology, for the first time, permitted direct abundance estimates of the argon (Monteiro & Dors 2021), neon (Armah et al. 2021), and helium (Dors et al. 2022) in the narrow-line regions (NLRs) of a large sample of Sy 2s. Generally, this class of AGN presents solar or oversolar metallicities ($12 + \log(O/H) \gtrsim 8.7$; e.g. Shields & Searle 1978; Groves, Heckman & Kauffmann 2006; Dors et al. 2020a) and gas with high ionization. These features make it possible to measure some auroral lines (e.g. [O III]λ4363, [N II]λ5755) in the high-metallicity regime, which are difficult to detect in SFs (e.g. van Zee et al. 1998; Díaz et al. 2007; Dors O. L. et al. 2008). However, it is worthwhile to point out some difficulties in applying the T_e method to derive abundances in AGNs, for instance: (i) due to the large width of Hγ, in several cases, this Balmer line is blended with the temperature-sensitive auroral line [O III]λ4363 in AGN spectra; (ii) although AGNs have a high ionization degree, its high metallicity (e.g. Groves et al. 2006) produces measurements of [O III]λ4363 with low signal-to-noise ratio (S/N), which translates into a large abundance uncertainty (e.g. Dors et al. 2022); and (iii) temperature estimates from distinct gas regions in AGNs are barely found in the literature, making it difficult to carry out any statistical study. In any case, with the current observational data and methodologies available in the literature it is possible to obtain (relatively) precise sulphur and oxygen abundances, producing important constraints to the studies of stellar nucleosynthesis in the high-metallicity regime. In fact, even the recent stellar nucleosynthesis models (e.g. Ritter et al. 2018) do not consider oversolar metallicities despite metallicity has an impact on the stellar product (e.g. Gronow et al. 2021).

Taking advantage of the availability of spectroscopic data of Sy 2s in the literature, data provided by the Sloan Digital Sky Survey (SDSS; York et al. 2000), and motivated by the new methodology proposed by Dors et al. (2020b), in this work, the last in a series of 10 papers, we present direct S and O abundance estimates for the NLRs of a sample of 45 Sy 2s. This study is organized as follows. In Section 2, the observational data are presented. The methodology used to estimate the sulphur and oxygen abundances is presented in Section 3. The results and discussion are given in Section 4. Finally, the key findings are summarized in Section 5.

---

[2]The metallicity in stars is usually traced by Fe/H abundance ratio (e.g. Allende Prieto et al. 2004).

2 OBSERVATIONAL DATA

In order to obtain a sample of Sy 2s with observational intensities of narrow (full width at half-maximum <1000 km s^{-1}) optical emission lines, we used spectroscopic data made available through the SDSS Data Release 17 (DR17; Abdurro'uf et al. 2022).[3] In this study, the procedures for selection of Sy 2s, emission-line measurements, reddening correction, and the stellar population continuum subtraction were the same as described by Dors et al. (2022), therefore, we summarized these processes below.

For each spectrum downloaded from the SDSS DR17, we performed the extinction correction using the Cardelli, Clayton & Mathis (1989) law assuming the parametrized extinction coefficient $R_V =$ 3.1. Thereafter, the stellar population continuum was subtracted from the spectra to obtain the pure nebular spectra using the stellar population synthesis STARLIGHT code (Cid Fernandes et al. 2005; Mateus et al. 2006; Vale Asari et al. 2016). The emission lines were fitted using the publicly available IFSCUBE package (Ruschel-Dutra & Dall'Agnol De Oliveira 2020; Ruschel-Dutra et al. 2021). The fluxes were corrected for extinction following the procedure described by Riffel et al. (2021b), where the observational Hα/Hβ line ratio was compared with the theoretical value (Hα/Hβ) = 2.86 proposed by Hummer & Storey (1987) for a temperature of 10 000 K and an electron density of 100 cm^{-3}. From the resulting sample, we selected only the objects that present the [O II]λ3726, λ3729 (hereafter [O II]λ3727), [O III]λ4363, Hβ, [O III]λ5007, Hα, [N II]λ6584, [S II]λ6716, λ6731, and [S III]λ9069 emission lines with an S/N higher than 2.0. Although the presence of the [N II]λ5755 and [S III]λ6312 auroral lines was not considered as selection criteria, when detected with (S/N) > 2 in the archival public data, their intensities were compiled.

Additionally, we also compiled from the literature emission-line intensities of Sy 2 nuclei obtained by different authors and applying the same selection criteria used for the SDSS data, with exception of the presence of the [S III]λ9069 line, which is not measured in most of the available data. In these cases, a cross-correlation was performed between the objects with optical data and those whose [S III]λ9069 was measured by Riffel, Rodríguez-Ardila & Pastoriza (2006), who presented a near-infrared (0.8–2.4 μm interval) spectral atlas of 47 AGNs. Initially, for each selected object, the [S III]λ9069 fluxes from Riffel et al. (2006) were divided by the Paβ flux. Thereafter, in order to obtain the [S III]λ9069 in relation to Hβ, the (Paβ/Hβ) = 0.162 theoretical ratio (Osterbrock 1989) was assumed for a temperature of 10 000 K and an electron density of 100 cm^{-3}. A similar procedure was performed by Binette et al. (2012).

Finally, for the entire sample, we applied the criterion proposed by Kewley et al. (2001),

$$\log([\text{O III}]\lambda5007/\text{H}\beta) > \frac{0.61}{\log([\text{N II}]\lambda6584/\text{H}\alpha) - 0.47} + 1.19,$$

(1)

to separate SF-like and AGN-like objects and the criterion proposed by Cid Fernandes et al. (2010),

$$\log([\text{O III}]\lambda5007/\text{H}\beta) > 0.47 + \log([\text{N II}]\lambda6584/\text{H}\alpha) \times 1.10,$$

(2)

to separate AGN-like and low-ionization nuclear emission-line region (LINER) objects. The final sample resulted in 45 Sy 2 nuclei,

[3]SDSS DR17 spectroscopic data are available at https://dr17.sdss.org/optical/plate/search.
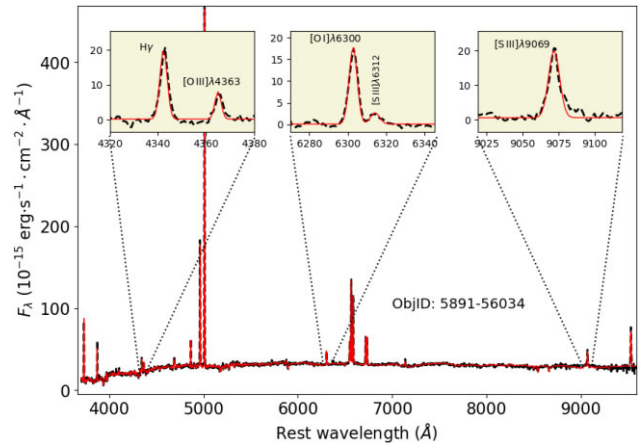

Figure 1. Optical spectrum (black colour) for one of the Seyfert 2 nuclei in our sample (see Section 2) obtained from the SDSS DR17. The fitting to the emission-line profiles using the IFSCUBE code is represented in red colour. The measured emission-lines and their corresponding wavelengths are indicated. Boxes show enlargements of regions around some weak lines, as indicated.

which is composed of 33 objects from SDSS data set (redshift $z < 0.08$) and 12 objects from the literature (redshift $z < 0.04$).

The reduced number of objects (33) resulting from the SDSS data base is mainly due to two selection criteria. First, the requirement for [O III]λ4363 measured at (S/N) > 2 makes it possible to select only 110 objects from a total of 333 Seyfert 2 nuclei. A similar sample size was obtained by Flury & Moran (2020), where the T_e method was applied in only 180 objects (see also Vaona et al. 2012; Dors et al. 2020a) selected from the SDSS Data Release 8 (DR8; Aihara et al. 2011). Second, the requirement for the presence of both [O II]λ3727 and [S III]λ9069 reduced our sample from 110 to only 33 objects. Izotov et al. (2006), who considered the SDSS Data Release 3 (DR3; Abazajian et al. 2005) data base to estimate elemental abundances in SFs, also reported the difficulty in measuring both [O II]λ3727 and [S III]λ9069 lines, mainly for galaxies at $z \lesssim 0.02$.

In Fig. 1, an example of a pure Sy 2 nebular spectrum (in black) from the SDSS sample and the fitting (in red) produced by the IFSCUBE package are shown. In Table A1, the reddening-corrected emission-line intensities (in relation to Hβ = 1.0) and the literature references from which the data were compiled are listed. In this table, the theoretical relation $I(\lambda9069) = 0.40 \times I(\lambda9532)$ between the [S III] emission lines is assumed.

In Fig. 2, a log([O III]λ5007/Hβ) versus log([N II]λ6584/Hβ) diagnostic diagram, the observational data, and the above criteria (equations 1 and 2) are shown. It can be seen that the Sy 2 sample covers a large range of ionization degree and metallicity, since a wide range of [O III]/Hβ and [N II]/Hα line ratio intensities is seen (e.g. Groves et al. 2006; Feltre, Charlot & Gutkin 2016; Carvalho et al. 2020).

The observational data sample is heterogeneous, in the sense that the spectra were obtained with distinct instrumentation (e.g. long-slit, fiber spectroscopy), aperture, reddening correction procedures, etc. These features could produce artificial scattering or biases in the derived abundances. Dors et al. (2020a, 2021) and Armah et al. (2021) presented a complete discussion on the use of a heterogeneous sample and its possible implications on abundance estimates. These authors pointed out that the effects of considering such a heterogeneous sample on abundance estimates produce uncertainties of ~0.1 dex, i.e. in the same order or even lower than those derived by applying the T_e method (e.g. Kennicutt et al. 2003; Hägele et al. 2008) and
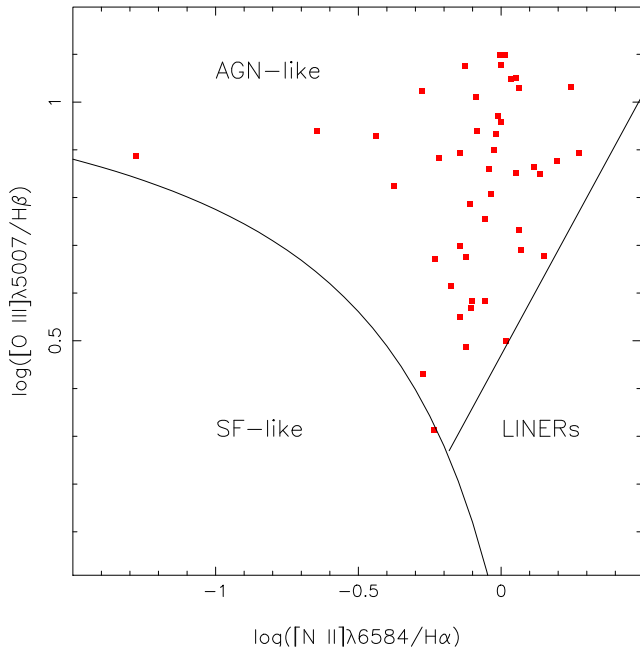
Figure 2. $\log([\text{O\,{\sc iii}}]\lambda 5007/\text{H}\beta)$ versus $\log([\text{N\,{\sc ii}}]\lambda 6584/\text{H}\alpha)$ diagnostic diagram. Red points represent the Sy 2 nuclei in our sample (see Section 2). The black solid curve represents the criterion (equation 1) proposed by Kewley et al. (2001) to separate AGN-like and SF-like objects. The black solid line represents the criterion (equation 2) proposed by Cid Fernandes et al. (2010) to separate AGN-like objects and LINERS.

strong-line methods (e.g. Storchi-Bergmann et al. 1998; Denicoló, Terlevich & Terlevich 2002). Moreover, Kewley, Jansen & Geller (2005) presented a detailed analysis of the effect of considering different apertures on the determinations of physical parameters of galaxies. These authors found that for aperture capturing less than 20 per cent of the total galaxy emission, the derived metallicity can differ by a factor of about 0.14 dex from the value obtained when the total galaxy emission is considered. However, only abundances of the nuclear regions are being considered here; therefore, the aperture effect on our estimates is not significant. Additional analysis of uncertainties in abundance estimates derived from distinct instrumentation and/or aperture has been addressed, for instance, by Mannucci et al. (2021), who analysed the diffuse ionized gas (DIG) contribution to the nebular emission of SFs. These authors, specifically, found that the [S\,{\sc ii}] line fluxes tend to be more affected in comparison with other optical line fluxes. Mannucci et al. (2021) also found that when spectra of local H\,{\sc ii} regions are extracted using large enough apertures while still avoiding the DIG, the observed line ratios are the same as in more distant galaxies. Therefore, there should not be any bias in our sample as a result of the usage of different instruments (see also Arellano-Córdova et al. 2022; Pilyugin et al. 2022). However, the requirement for the presence of the weak [O\,{\sc iii}]$\lambda 4363$ line (about 100 times weaker than Hβ) in the SDSS spectra yields a bias in our analysis, in the sense that objects with very high metallicity, where the gas suffers strong cooling and the electron temperature is low enough not to produce significant emission of this line, are mostly excluded. In fact, for instance, Dors et al. (2020a) selected from the SDSS DR7 data base (Abazajian et al. 2009), 463 confirmed Sy2 spectra with only 150 objects having [O\,{\sc iii}]$\lambda 4363$ measured with $(S/N) > 2$ and from these, only 36/150 have oversolar metallicity according to the T_e method applied by Dors et al. (2020b). Thus, abundance determinations obtained in this study do not extend to

objects with the highest expected metallicity (see also van Zee et al. 1998; Izotov et al. 2006; Flury & Moran 2020).

Another issue is the SF emission contribution to our AGN spectra, which can have a greater impact on the observed line fluxes for the most distant objects. Davies et al. (2014) presented a spatially resolved study of the active galaxy NGC 7130 ($z = 0.016$) and found that SFs are responsible for 30 per cent and 65 per cent of the [O\,{\sc iii}] and Hα luminosity, respectively. Moreover, Vidal-García et al. (2022) compared results from the NLR photoionization models (Feltre et al. 2016) incorporated into the BEAGLE (Bayesian spectra energy distribution – SED – fitting; Chevallard & Charlot 2016) code with observational spectroscopic data and showed that the SF Hβ flux contribution to the total nuclear flux of an active galaxy can range from 0 per cent to 50 per cent. However, we emphasize that, in principle, the SF flux contribution has a minimal effect on AGN abundance estimates when a sample of objects is considered. This assertion is supported by Thomas et al. (2019), who demonstrated that the aperture effect (and consequently SF contribution) has a negligible impact on metallicity estimates once comparable mass–metallicity relations for galaxies in four redshift bins were considered.

Since the [S\,{\sc iii}] lines of Seyfert galaxies are rarely found in the literature due to the fact that they are located in the near-infrared that there are few instruments operating, it is worthwhile to compare their emission-line flux ratios with those of SFs. In this regard, we consider emission-line intensities of H\,{\sc ii} galaxies (44 objects) and giant H\,{\sc ii} regions (GHRs, 34 objects) presented by Hägele et al. (2006, 2008, 2011, 2012). Besides, we compare the Sy 2 emission lines considered in this work with those from 378 disc H\,{\sc ii} regions located in six local spiral galaxies, which have been made available by the CHAOS project,[4] and presented by Berg et al. (2015, 2020), Croxall et al. (2015, 2016), and Rogers et al. (2021, 2022). This comparison (see also Díaz & Zamora 2022) is shown in Fig. 3. A clear correlation is derived between the two data set since both line ratios are dependent on the ionization degree of the gas. Interestingly, Sy 2 nuclei present similar [S\,{\sc iii}]/[S\,{\sc ii}] line ratio intensities to those of SFs. The Sy 2 [O\,{\sc iii}]/[O\,{\sc ii}] line ratio intensities are in consonance with those of H\,{\sc ii} galaxies and GHRs and are higher than those from disc H\,{\sc ii} regions.

3 ABUNDANCE ESTIMATES

For the Sy 2 sample previously described, we determined the sulphur and oxygen abundances relative to hydrogen. To do that, electron temperatures representing the zones where distinct ions are located in the gas phase, electron density, and ionic abundances were calculated using the 1.1.13 version of PYNEB code (Luridiana et al. 2015), which permits an interactive procedure in the derivation of these parameters. The references for the predefined atomic parameters incorporated into the PYNEB code are listed in Table 1.

As the line measurements for some objects (9/45) of our sample do not present observational errors, the abundance uncertainties were estimated using Monte Carlo simulations. For each diagnostic line, we generate 1000 random values assuming a Gaussian distribution with a standard deviation equal to the associated uncertainty of 10 per cent and 20 per cent for strong (e.g. [O\,{\sc iii}]$\lambda 5007$) and auroral (e.g. [O\,{\sc iii}]$\lambda 4363$) line intensities involved in the diagnostics, respectively. Thereafter, an empirical ICF was considered in the derivation of the total sulphur abundance. For objects that have
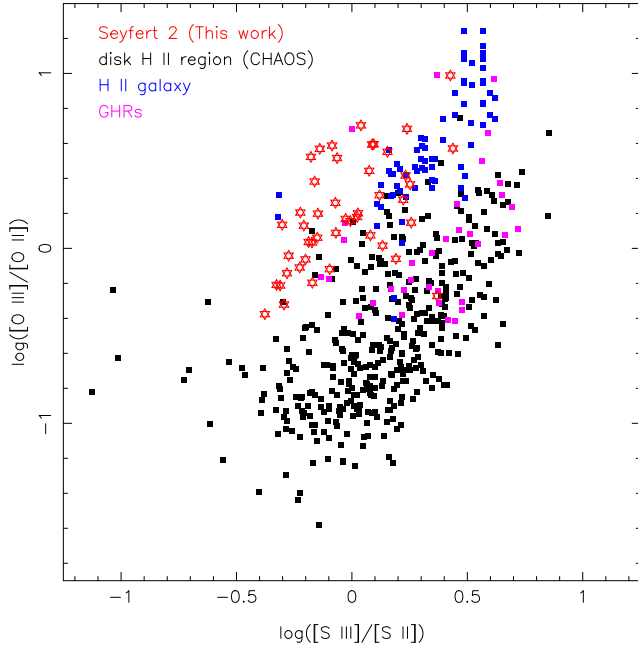
---

[4]https://www.danielleaberg.com/chaos

Figure 3. Logarithm of [O III]λ5007/[O II]λ3727 versus [S III]λ9069 + λ9532/[S II]λ6716 + λ6731. Red points represent the Sy 2 sample (see Section 2) whose emission line intensities are listed in Table A1. Black points represent disc H II regions whose data were taken from the CHAOS project and obtained by Berg et al. (2015, 2020), Croxall et al. (2015, 2016), and Rogers et al. (2021, 2022). Blue points represent H II galaxies taken from Hägele et al. (2006, 2008, 2011, 2012), and pink points represent GHRs taken from Hägele et al. (2006).

measured emission-line errors (36/45), the uncertainties in the final abundance values were obtained propagating the errors in the line measurements, electron temperature, and electron density. Subsequently, the description of the employed methodology is presented.

3.1 Temperature estimations

Several studies have been directed to estimate the chemical composition of SFs and, in almost all of these estimates, it has been a common practice to use temperature relations derived from photoionization models to infer the temperatures in the unobserved ionization zones (e.g. Stasińska 1990; Garnett 1992; Pérez-Montero & Díaz 2003; Izotov et al. 2006). However, when temperature relations predicted by photoionization models simulating SFs are compared with direct estimates relying on auroral lines, large deviations are found, reaching up to ∼5000 K (e.g. Hägele et al. 2008; Arellano-Córdova & Rodríguez 2020; Berg et al. 2020). Despite the fact that temperature relations for AGNs are barely found in the literature (see Dors et al. 2020b; Armah et al. 2021; Monteiro & Dors 2021), it seems that similar disagreement is also derived for this class of object. In fact, Riffel et al. (2021a) compared the $T_e(N^+)$–$T_e(O^{2+})$ relation predicted by photoionization models, built using the CLOUDY code (Ferland et al. 2013), with values derived from observational auroral emission lines for a sample of 12 local Seyfert nuclei. The model predictions reproduce the direct temperature observations for all objects, except for Mrk 348 for which the direct $T_e(N^+)$ value is ∼10 000 K higher than the predicted one. This object is know to host ionized gas outflows (Freitas et al. 2018) and probably the higher observed temperatures are due to extra heating caused by shocks (see Dors et al. 2021), which is not accounted in the photoionization

models considered by Riffel et al. (2021a). Obviously, additional comparison with a larger sample of objects combined with kinematic studies (e.g. Xu et al. 2021; Flury et al., in preparation) of objects, where gas outflow is detected, is necessary to confirm this result.

Since comparisons between observational emission-line intensities and the ones predicted by photoionization models indicate that the main ionization source of most NLR of Sy 2s is the radiation emitted by gas accretion into a supermassive black hole, for objects in the local universe (see e.g. Stasińska 1984; Ferland & Osterbrock 1986; Storchi-Bergmann et al. 1998; Groves et al. 2006; Feltre et al. 2016; Castro et al. 2017; Dors et al. 2017, 2020b; Pérez-Montero et al. 2019; Thomas et al. 2019; Carvalho et al. 2020; Armah et al. 2021) and also at high redshift (see e.g. Nagao, Maiolino & Marconi 2006; Matsuoka et al. 2009, 2018; Dors et al. 2014, 2018, 2019; Nakajima et al. 2018; Mignoli et al. 2019; Guo et al. 2020), we are able to apply the T_e method to derive reliable estimates. However, the weak temperature-sensitive auroral emission-line measurements are barely available in the literature for AGNs, therefore we developed our own empirical method based on our sample.

To derive the empirical relations for our abundance estimates, we used auroral line intensities from our sample and those of Sy 2 NLRs available in the literature. First, the observational intensities of the RO3 = [O III](λ4959 + λ5007)/λ4363 and RN2 = [N II](λ6548 + λ6584)/λ5755 line ratios were used to calculate $T_e(O^{2+})$ and $T_e(N^+)$, respectively, for 18 objects, i.e. seven objects of our sample (see Table A1) and 11 Sy 2 compiled by Dors et al. (2020b). To derive $T_e(S^{2+})$, we used the RS3 = [S III](λ9069 + λ9532)/λ6312 line ratios for 14 objects (over 45) in our sample (see Table A1). For each object, the temperature estimates were performed assuming a constant electron density (N_e) value across the nebula, which is derived from the RS2 = [S II]λ6716/λ6731 intensity ratio. In Table 2, the objects and their corresponding RO3, RN2, RS3, and RS2 line intensities ratios, the electron density, $T_e(O^{2+})$, $T_e(N^+)$, and $T_e(S^{2+})$ temperature derived values are listed. We note that the object 56067−0382 has a $T_e(N^+)$ higher than those derived for other objects and similar to the value derived for Mrk 348 by Riffel et al. (2021a). Probably 56067−0382 presents gas outflows but its temperatures were still considered. Since in most cases only the [O III]λ4363 auroral line is measured (e.g. van Zee et al. 1998; Kennicutt et al. 2003), we proposed, as usual, temperature relations with respect to $T_e(O^{2+})$. In Fig. 4, $T_e(N^+)$ and $T_e(S^{2+})$ are plotted against $T_e(O^{2+})$, with the values in units of 10^4 K. In the upper panel of this figure, the dashed line represents the equality between $T_e(S^{2+})$ and $T_e(O^{2+})$. As for SFs (e.g. see Hägele et al. 2008; Berg et al. 2020), clear correlations between the Sy 2 temperatures are observed, with a linear regression resulting in

$$t_e(N^+) = 0.36(\pm 0.23) \times t_e(O^{2+}) + 0.55(\pm 0.39) \quad (3)$$

and

$$t_e(S^{2+}) = 2.23(\pm 1.12) \times t_e(O^{2+}) - 0.74(\pm 1.34), \quad (4)$$

where $t_e = T_e/10^4$ K.

It can be seen in Fig. 4 that higher temperature values for S^{2+} are derived in comparison with those for O^{2+}, probably indicating that the former ion occupy an inner gas region than the latter. Conversely, an opposite result is derived for disc H II regions, i.e. $T_e(O^{2+})$ is ∼1000 K higher than $T_e(S^{2+})$ (e.g. Rogers et al. 2021). Hägele et al. (2006) analysed the relation between $T_e(O^{2+})$ and $T_e(S^{2+})$ using a sample that comprises H II galaxies, giant extragalactic H II regions, Galactic H II regions, and H II regions from the Magellanic Clouds (MCs). These authors found that the [S III] electron temperatures are higher than the corresponding [O III] estimations for most objects

Table 1. Atomic data set used for collisionally excited lines of selected element ions.

Ion	Transition probabilities	Collisional strengths
S^+	Froese Fischer, Tachiev & Irimia (2006)	Tayal & Zatsarinny (2010)
S^{2+}	Froese Fischer et al. (2006)	Tayal & Gupta (1999)
O^+	Wiese, Fuhr & Deters (1996)	Kisielius et al. (2009)
O^{2+}	Froese Fischer & Tachiev (2004), Storey & Zeippen (2000)	Storey, Sochi & Badnell (2014)

Table 2. Estimates of $T_e(O^{2+})$, $T_e(N^+)$, and $T_e(S^{2+})$ used to obtain the relations given by equations (3) and (4). The line ratios are: RO3 = ([O III]$\lambda4959 + \lambda5007)/\lambda4363$, RN2 = ([N II]$\lambda6548 + \lambda6584)/\lambda5755$, RS3 = ([S III]$\lambda9069 + \lambda9532)/\lambda6312$, and RS2 = [S II]$\lambda6716/\lambda6731$.

Object	RO3	RN2	RS3	RS2	$T_e(O^{2+})$ (K)	$T_e(N^+)$ (K)	$T_e(S^{2+})$ (K)	N_e (cm^{-3})	Ref.
IZw 92	42.62 ± 8.52	66.50 ± 13.30	–	0.92 ± 0.09	16 350 ± 1646	9929 ± 788	–	1176 ± 427	1
Mrk 3	69.41 ± 13.88	87.29 ± 17.45	–	0.89 ± 0.08	13 151 ± 1059	8969 ± 638	–	1221 ± 395	2
Mrk 78	112.90 ± 22.58	95.31 ± 19.06	–	1.11 ± 0.11	11 023 ± 743	8754 ± 607	–	467 ± 229	2
Mrk 34	100.90 ± 20.18	87.27 ± 17.45	–	1.02 ± 0.10	11 445 ± 800	9012 ± 643	–	691 ± 280	2
Mrk 1	69.09 ± 13.81	135.45 ± 27.09	–	0.94 ± 0.09	13 187 ± 1060	7773 ± 481	–	1000 ± 362	2
Mrk 533	95.00 ± 19.00	240.00 ± 48.00	–	0.86 ± 0.08	11 681 ± 834	6591 ± 346	–	1319 ± 429	3
Mrk 612	60.00 ± 12.00	112.00 ± 22.40	–	1.36 ± 0.13	13 993 ± 1199	8304 ± 551	–	87 :	3
ESO 138 G1	34.23 ± 6.84	47.73 ± 9.54	–	0.97 ± 0.09	18 386 ± 2084	11 457 ± 1055	–	1003 ± 366	4
NGC 2992	40.36 ± 8.07	98.20 ± 19.64	–	1.12 ± 0.11	16 831 ± 1736	8659 ± 595	–	514 ± 266	5
NGC 2210	24.36 ± 4.87	117.77 ± 23.55	–	1.06 ± 0.10	22 797 ± 3095	8143 ± 527	–	744 ± 328	5
NGC 5506	73.57 ± 14.70	168.50 ± 33.70	–	0.92 ± 0.09	12 859 ± 1012	7279 ± 421	–	1074 ± 386	5
Mrk 348	23.7 ± 2.4	31.8 ± 11.9		0.83 ± 0.03	28 600 ± 4700	21 700 ± 6100	–	1940 ± 245	6
Mrk 607	29.7 ± 10.2	80.6 ± 16.2		0.87 ± 0.11	23 500 ± 2700	10 200 ± 1300	–	1548 ± 707	6
56067−0382	41.43 ± 8.29	12.29 ± 2.46	–	1.06 ± 0.16	16 604 ± 1694	31 367 ± 8555	–	669 ± 463	7
55539−0167	82.20 ± 16.44	24.49 ± 4.90	–	1.13 ± 0.17	12 334 ± 928	16 655 ± 2244	–	442 ± 349	7
56001−0293	109.00 ± 21.80	37.02 ± 7.40	–	1.39 ± 0.21	11 159 ± 760	13 147 ± 1393	–	58 :	7
55742−0383	99.80 ± 19.96	42.04 ± 8.41	–	1.13 ± 0.17	11 497 ± 806	12 245 ± 1202	–	432 ± 340	7
55302−0655	41.20 ± 8.24	47.71 ± 9.54	–	1.24 ± 0.19	16 672 ± 1708	11 537 ± 1068	–	266 ± 0	7
56568−0076	105.33 ± 21.07	96.13 ± 19.23	–	1.03 ± 0.15	11 280 ± 780	8715 ± 604	–	660 ± 407	7
56566−0794	94.80 ± 18.96	127.06 ± 25.41	4.36 ± 0.87	1.18 ± 0.18	11 713 ± 838	7968 ± 505	21 665 ± 3991	342 :	7
55181−0154	130.33 ± 26.07	–	3.85 ± 0.77	0.98 ± 0.15	10 508 ± 675	–	24 380 ± 5015	786 ± 474	7
56088−0473	128.33 ± 25.67	–	18.00 ± 3.60	1.09 ± 0.16	10 566 ± 682	–	9244 ± 747	502 ± 349	7
56034−0154	84.86 ± 16.97	–	12.00 ± 2.40	1.09 ± 0.16	12 184 ± 909	–	11 052 ± 1070	527 ± 370	7
56626−0636	102.00 ± 20.40	–	3.49 ± 0.70	1.08 ± 0.16	11 409 ± 795	–	27 079 ± 6116	537 ± 371	7
55651−0052	177.00 ± 35.40	–	5.37 ± 1.07	1.06 ± 0.16	9576 ± 560	–	18 131 ± 2884	549 ± 368	7
56206−0454	74.11 ± 14.82	–	6.17 ± 1.23	1.23 ± 0.18	12 842 ± 1010	–	16 315 ± 2354	267 :	7
55860−0112	71.09 ± 14.22	–	3.39 ± 0.68	1.02 ± 0.15	13 038 ± 1038	–	27 975 ± 6506	724 ± 448	7
55710−0116	107.71 ± 21.54	–	12.29 ± 2.46	0.92 ± 0.14	11 189 ± 764	–	10 917 ± 1047	1018 ± 578	7
56366−0928	47.50 ± 9.50	–	3.14 ± 0.63	1.00 ± 0.15	15 523 ± 1474	–	30 648 ± 7717	834 ± 517	7
56328−0550	81.67 ± 16.33	–	7.48 ± 1.50	1.28 ± 0.19	12 373 ± 934	–	14 339 ± 1821	190 :	7
55617−0758	76.80 ± 15.36	–	3.45 ± 0.69	0.90 ± 0.13	12 640 ± 978	–	27 394 ± 6222	1156 ± 609	7
56003−0218	67.14 ± 13.43	–	5.89 ± 1.18	0.97 ± 0.14	13 337 ± 1088	–	16 867 ± 2531	889 ± 504	7
55505−0654	198.75 ± 39.75	–	12.00 ± 2.40	1.12 ± 0.17	9268 ± 524	–	11 052 ± 1072	422 ± 319	7

Note. References: 1 – Kraemer et al. (1994); 2 – Koski (1978); 3 – Shuder & Osterbrock (1981); 4 – Alloin et al. (1992); 5 – Shuder (1980); 6 – Riffel et al. (2021a); and 7 – SDSS sample.

presenting temperatures higher than about 14 000 K, mainly the metal-poor H II galaxies, and the opposite behaviour for the coolest nebulae, mainly giant extragalactic H II regions, Galactic H II regions, and H II regions from the MCs, which present the highest metallicities. Taking into account the temperatures of the different samples studied by Hägele et al. (2008, H II galaxies that present the higher temperatures) and Rogers et al. (2021, galactic disc H II regions with lower temperatures), the $T_e(S^{2+})$–$T_e(O^{2+})$ behavior derived in this paper for Sy 2s is the same as found by Hägele et al. (2006).

Spatially resolved observational studies of NLRs have found a profile of electron density along the AGN radius, in the sense that denser gas is located in the inner regions. For instance, Freitas et al. (2018), who obtained emission-line flux of two-dimensional maps from five bright nearby Seyfert nuclei, obtained electron densities ranging from ∼2500 cm^{-3} in the central parts to ∼100 cm^{-3} in the

outskirts (see also Kakkad et al. 2018; Revalski et al. 2018a,b, 2021, 2022; Mingozzi et al. 2019; Ruschel-Dutra et al. 2021). Moreover, electron density estimations through the [Ar IV]$\lambda4711/\lambda4740$ line ratio, which traces the density in the innermost layers, showed values of up to ∼13 000 cm^{-3} (e.g. Congiu et al. 2017; Cerqueira-Campos et al. 2021). Thus, density values derived from [S II] lines may not be representative of the region where S^{2+} ions are located, which could inherently introduce an error in the $T_e(S^{2+})$ values. In order to explore the influence of the electron density on the sulphur temperature estimations, we show in Fig. 5 the $t_e(S^{2+})$ derived assuming the N_e values from [S II]$\lambda6716/\lambda6731$ line ratios (listed in Table 2) versus the estimations considering a fixed value of 13 000 cm^{-3}, as derived by Congiu et al. (2017) for the extended NLR of the Seyfert 2 galaxy IC 5063. We notice a good agreement between the values, with a difference of ∼2 per cent, which is lower than the uncertainty
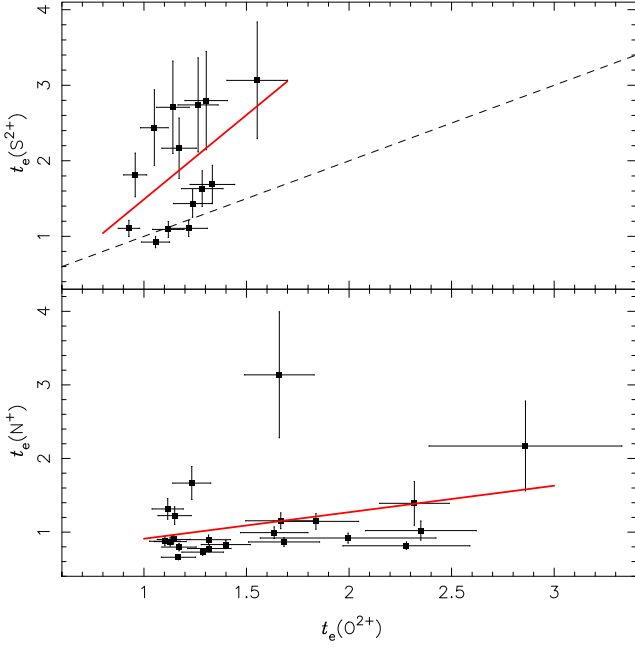
Figure 4. Comparing direct temperature values for different ions. Values are in units of 10^4 K. Botton panel: $t_e(O^{2+})$ and $t_e(N^+)$ are derived through the RO3 = [O III](λ4959 + λ5007)/λ4363 and RN2 = [N II](λ6548 + λ6584)/λ5755 line intensities ratios, respectively, and the electron density (from the RS2 = [S II]λ6716/λ6731) listed in Table 2, and by using version 1.1.13 of PYNEB code (Luridiana et al. 2015). The red line represents the linear regression to the points given by equation (3). Top panel: same as bottom panel but for $t_e(S^{2+})$ values derived from RS3 = [S III](λ9069 + λ9532)/λ6312. Red line represents the linear regression to the points given by equation (4) while the dashed line the equality between the estimates.
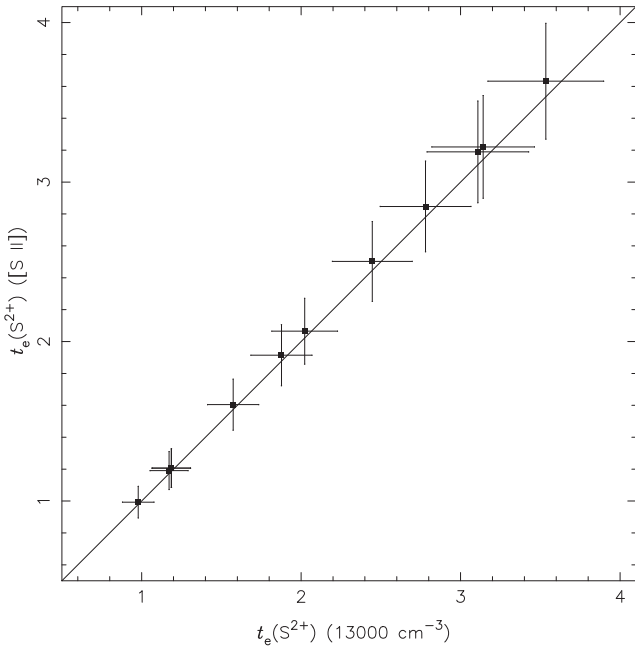

Figure 5. Comparison between electron temperatures (in units of 10^4 K) derived from the RS3 = [S III](λ9069 + λ9532)/λ6312 assuming electron density estimations via the RS2 = [S II]λ6716/λ6731 (listed in Table 2) with the estimates assuming a value of 13 000 cm^{-3} as derived by Congiu et al. (2017) from [Ar IV]λ4711/λ4740. Line represents the equality between the two estimates.

Table 3. Critical densities for collisional deexcitation for the lines involved in this work. Values were calculated with the PYNEB code (Luridiana, Morisset & Shaw 2015) assuming an electron temperature of 15 000 K.

Line	N_c (cm^{-3})
[O II]λ3726	4.72×10^3
[O II]λ3729	1.49×10^3
[O III]λ4363	2.88×10^7
[O III]λ5007	7.83×10^5
[N II]λ5755	1.87×10^7
[S III]λ6312	1.44×10^7
[N II]λ6484	1.04×10^5
[S II]λ6716	1.37×10^3
[S II]λ6731	3.67×10^3
[S III]λ9069	6.42×10^5

produced by the error in the line measurements ($\sim$10 per cent, see Table 2). In Table 3, the critical density (N_c) values for the lines involved in this work, calculated with the PYNEB code (Luridiana et al. 2015) assuming an electron temperature of 15 000 K, are listed. One can see that N_c values are higher than the electron density values (listed in Table A2) derived for our Sy 2 sample. Thus, electron density variations in NLRs have a minimal influence on our temperature estimates. For some objects, the emission-line errors are significant, thus frequently with density error bars larger than the determinations themselves. Therefore we use ':' to indicate that error bars are at least an order of magnitude larger than the expected density (see Table A2).

Because of the similarity among the S^+, N^+, and O^+ ionization potentials (23.33, 29.60, and 35.12 eV, respectively) and because the [S II]$\lambda\lambda$4068, 4076 and [O II]$\lambda\lambda$7320, 7330 auroral lines are not measured in our sample of spectra, as in Rogers et al. (2021), we adopted $T_e(S^+) = T_e(O^+) = T_e(N^+)$. In objects for which it is possible to estimate directly $T_e(N^+)$ (7/45) and $T_e(S^{2+})$ (14/45), these temperatures were assumed as representative of the low- and high-ionization zones, respectively. Otherwise, when the [N II]λ5755 and [S III]λ6312 auroral emission-line measurements are not available, $T_e(N^+)$ and $T_e(S^{2+})$ were derived from the equations (3) and (4), respectively. In Table A2, electron density and temperature values for the objects in our sample are presented.

3.2 Abundance derivation

For each object of our sample, using the emission-line intensity ratios listed in Table A1, the electron temperature and electron density values (listed in Table A2), as well as the PYNEB code (Luridiana et al. 2015), we derived the sulphur (S^+, S^{2+}) and oxygen (O^+, O^{2+}) ionic abundances. Afterwards, applying an empirical ICF for the sulphur and a typical value for the oxygen ICF, the total abundances for the S/H and O/H were estimated. In what follows, we describe the methodology employed in the derivation of the abundance of each considered element.

3.2.1 Oxygen abundance

The total oxygen abundance in relation to the hydrogen one was derived assuming

$$\frac{O}{H} = ICF(O^+ + O^{2+}) \times \left[\frac{O^+}{H^+} + \frac{O^{2+}}{H^+} \right], \quad (5)$$

where ICF($O^+ + O^{2+}$) represents the ionization correction factor for oxygen that takes into account the contribution of unobservable

oxygen ions, whose emission lines are observed in other spectral bands such as X-rays (e.g. Cardaci et al. 2009, 2011; Bianchi et al. 2010; Bogdán et al. 2017; Maksym et al. 2019; Kraemer et al. 2020) and infrared (e.g. Diamond-Stanic & Rieke 2012; Fernández-Ontiveros et al. 2016). The O^{2+}/H^+ ionic abundance was calculated by using the [O III]λ5007/Hβ line ratio and assuming the direct $T_e(O^{2+})$ and N_e values derived from RO3 and RS2, respectively. The O^+/H^+ abundance was calculated from the [O II]λ3727/Hβ emission line ratio and assuming $T_e(O^+) = T_e(N^+)$ with $T_e(N^+)$ estimated from the empirical relation given by equation (3) when the [N II]λ5755 auroral emission-line measurement is not available.

To derive ICF($O^+ + O^{2+}$) it is necessary to calculate the He^+/H^+ and He^{2+}/H^+ ionic abundances (e.g. Torres-Peimbert & Peimbert 1977; Izotov et al. 2006; Flury & Moran 2020), which is not possible because in most of the AGN spectra from our sample, the helium recombination line λ4686 Å is not measured. Therefore, for consistency, the ICF($O^+ + O^{2+}$) is assumed to have a value of 1.50 for all objects, which is an average value derived by Dors et al. (2022), who found ICF values ranging from 1.30 to 1.70 for a sample of 65 local ($z \lesssim 0.2$) Sy 2s. This ICF value translates into an abundance correction of $\sim$0.2 dex, i.e. somewhat higher than the uncertainty ($\sim$0.1 dex) of abundances usually relied on for the T_e method (e.g. Kennicutt et al. 2003; Hägele et al. 2008).

3.2.2 Sulphur abundance

The S^+/H^+ ionic abundance for each object of our sample was derived by using the [S II](λ6716 + λ6731)/Hβ line intensities ratio and assuming $T_e(S^+) = T_e(N^+)$, where $T_e(N^+)$ was calculated from equation (3) when the [N II]λ5755 auroral emission-line measurement is not available. Because of the similarity between the ionization potentials of S^+ and N^+ (23.33 and 29.60 eV, respectively), these ions are approximately located in the same gas region and the use of a common temperature for both is a good approach as largely used in SF chemical abundance studies (e.g. Kennicutt et al. 2003). However, Rogers et al. (2021), who compared SF direct estimates of $T_e(S^+)$ [derived from RAS2 = [S II](λ6716 + λ6731)/(λ4068 + λ4074)] with $T_e(N^+)$ [derived from RN2 = [N II](λ6548 + λ6584)/(λ5755)], found somewhat higher $T_e(S^+)$ values than $T_e(N^+)$, with an intrinsic dispersion of $\sim$950 K between these temperatures. Unfortunately, RAS2 values for Sy 2 are rarely found in the literature thus far, which makes it impossible to verify whether any of these conclusions also apply to AGNs.

Similarly, the S^{2+}/H^+ was derived by using the [S III]λ9069/Hβ line intensities ratio listed in Table A1 and the $T_e(S^{2+})$ values from equation (4) when the RS3 line ratio is not available. The uncertainties associated with the sulphur ionic estimates is mainly due to the error in the measurements of the emission-line fluxes and the uncertainties in the temperature values. In Table A3, the sulphur ionic abundance values for each object of the sample are listed.

The total sulphur abundance in relation to the hydrogen one was considered to be

$$\frac{S}{H} = ICF(S^+ + S^{2+}) \times \left[\frac{S^+}{H^+} + \frac{S^{2+}}{H^+} \right], \tag{6}$$

where ICF($S^+ + S^{2+}$) is the ionization correction factor for sulphur. Since AGNs have harder ionizing sources than typical SFs (e.g. Feltre et al. 2016), it is expected that the gas phase of these objects contains the presence of ions with higher ionization level than S^{2+}. In fact, [S VIII]λ9910 and [S IX]λ12520 emission lines were observed in large number of AGNs in the sample presented by Riffel et al. (2006). However, measurements of S^{3+} lines (e.g. [S IV]10.51 µm)
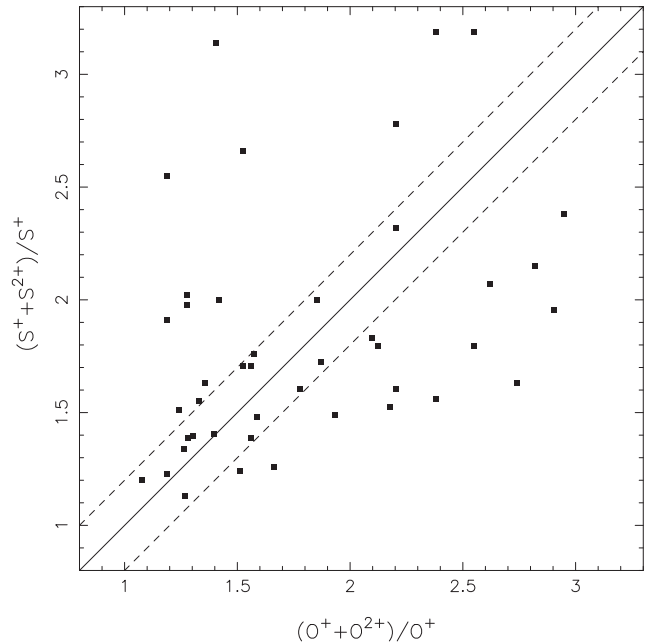

Figure 6. Sulphur versus oxygen ionic abundance ratios for our sample of objects (see Section 2) calculated via the T_e method (see Section 3). Solid line represents the equality between the estimates. Dashed lines correspond to the deviation of 20 per cent from the one–one relation representing the mean error in the ionic abundance estimations.

are not available in the literature, which makes it impossible for the derivation of an empirical ICF(S) for AGNs, such as derived for SFs by Dors et al. (2016).

The first ICF for sulphur (likewise for other elements) was proposed for SFs by Peimbert & Costero (1969) and it is given by

$$ICF(S^+ + S^{2+}) = \frac{S^+ + S^{2+}}{S^+} = \frac{O^+ + O^{2+}}{O^+}. \tag{7}$$

Rogers et al. (2021) tested the application of this ICF for SFs (see also Díaz & Zamora 2022) and pointed out that it is particularly reliable for low ionization degree, i.e. when O^+ zone is more dominant than the O^{2+} zone [(O^+/O) > 0.6]. Hitherto, there has not been sulphur ICFs for AGNs in the literature and it is unknown if the above relation is completely valid for this object class. Therefore, in order to ascertain whether the sulphur ICF can be applied to Sy 2s, we performed a simple test to verify the equality indicated in equation (7). The ionic ratios for our sample are plotted in Fig. 6, where the black solid line represents the equality between the estimates, while the dashed lines represent the deviations of 20 per cent from the one–one relation. It can be seen that, despite the scattering, most of the ionic abundance ratio estimates are located around of the one–one relation. Thus, we assumed as valid the equation (7) for NLR sulphur abundance estimates.

Ionic and total oxygen and sulphur abundance estimates derived through the T_e method together with the sulphur ICFs for each object in our sample are listed in Table A3.

4 RESULTS AND DISCUSSION

4.1 Temperature estimates

Recent studies of spatially resolved central parts of galaxies have uncovered the temperature structure of a few AGNs. For instance,

Revalski et al. (2021), using *Hubble Space Telescope* and Apache Point Observatory spectroscopy, obtained direct estimates of $T_e(O^{2+})$ along the radius of the Sy 2 nucleus of Mrk 78 and found temperatures in the range 10 000–15 000 K, with no systematic variation (see also Revalski et al. 2018a,b). Riffel et al. (2021c) used Gemini Multiobject Spectrograph (GMOS)-Integral Field Unit (IFU) observations of three luminous nearby Seyfert galaxies (Mrk 79, Mrk 348, and Mrk 607) and estimated $T_e(O^{2+})$ fluctuations in the inner 0.4–1.1 kpc region of these galaxies. These authors found temperature fluctuations similar to those derived in SFs and PNe. Despite the revelations provided by these recent studies, an advance in the understanding of the temperature structure of AGNs, additional point-to-point or integrated T_e estimates through distinct emission lines [e.g. [S III](λ9069 + λ9532)/λ6312 and [N II](λ6548 + λ6584)/λ5755] are rare in the literature, prompting further investigation of the AGN temperature structure. Thus, our temperature estimates provide valuable knowledge to the nature of NLRs.

A large number of AGNs present gas outflows (e.g. Riffel et al. 2020; Armus et al. 2023), shocks (e.g. Aldrovandi & Contini 1984; Dopita & Sutherland 1995; Dors et al. 2021), and neutral gas reservoirs that can coexist with the ionized gas (e.g. García-Burillo et al. 2014) and, in combination with the hard ionization source (e.g. Feltre et al. 2016), tend to produce a more complex gas structure than that of SFs (e.g. Hägele et al. 2006; García-Benito et al. 2010; Pérez-Montero et al. 2011; Monreal-Ibero, Walsh & Vílchez 2012; Durré & Mould 2018). However, complex temperature structures can also be observed in SFs (e.g. Dopita et al. 2005; Jin, Kewley & Sutherland 2022) produced, for instance, by starburst-driven outflows cooling (e.g. Danehkar, Oey & Gray 2022). On the scenario where distinct physical processes drive the gas structure, it is expected that temperature relations of AGNs tend to differ from the ones derived for SFs. In order to test this hypothesis, in Fig. 7, we compare our Sy 2 temperature estimates and empirical relations (equations 3 and 4) with those derived for SFs by the following authors.

(i) Hägele et al. (2006): these authors used their own high-quality spectra of H II galaxies and a large literature compilation of H II galaxies, giant extragalactic H II regions, Galactic H II regions, and H II regions from the MCs performed by Pérez-Montero et al. (2006) to analyse the relation between $T_e(O^{2+})$ and $T_e(S^{2+})$ values derived using the T_e method (see fig. 7 of Hägele et al. 2006). Their linear fitting to the complete sample gave the relation

$$t_e(S^{2+}) = 1.19(\pm 0.08) \times t_e(O^{2+}) - 0.32(\pm 0.10), \qquad (8)$$

which has a validity range of $0.70 \lesssim t_e(O^{2+}) \lesssim 2.0$.

(ii) Rogers et al. (2021): the estimates by these authors include temperature values obtained for a large number of disc H II regions in the spiral galaxy NGC 2403 using the T_e method. These estimates combined with those of H II regions in four spiral galaxies (see fig. 3 by Rogers et al. 2021) resulted in the relations

$$t_e(N^+) = 0.79(\pm 0.14) \times t_e(O^{2+}) + 0.16(\pm 0.13) \qquad (9)$$

and

$$t_e(S^{2+}) = 1.58(\pm 0.17) \times t_e(O^{2+}) - 0.57(\pm 0.16), \qquad (10)$$

which are valid for $0.70 \lesssim t_e(O^{2+}) \lesssim 1.5$.

(iii) Arellano-Córdova & Rodríguez (2020): these authors compiled emission-line intensities of H II regions from the literature to explore the behaviour of the $T_e(N^+)$–$T_e(O^{2+})$ temperature relation. These authors found that this relation has a dependence on the gas ionization degree, which is traced by the line ratio $P = ([1 III]\lambda 4959 + \lambda 5007)/[1 II]\lambda 3727 + [1 III]\lambda 4959 +$
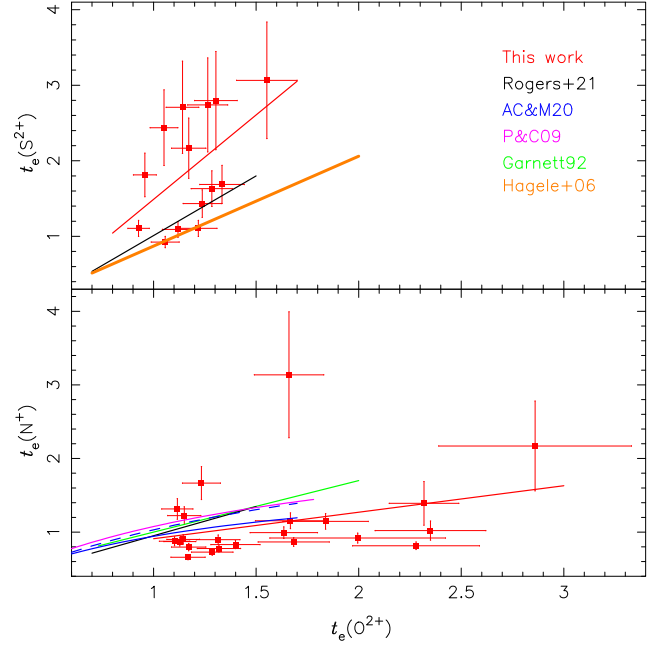

Figure 7. Same as Fig. 5 but comparing our temperature estimates (red points) and temperature relations (red lines represented by equations 3 and 4) with relations obtained from SFs. Orange solid line plots the empirical relation (equation 8) obtained by Hägele et al. (2006) using direct temperature estimates for a large sample of H II galaxies, giant extragalactic H II regions, Galactic H II regions, and H II regions from the MCs. Black solid lines represent the empirical relations (equations 9 and 10) based on direct estimates of disc H II regions by Rogers et al. (2021). Blue dashed and solid lines, shown only in bottom panel, represent empirical relations for $P < 0.5$ and for $P > 0.5$, respectively, based on data compiled from literature by Arellano-Córdova & Rodríguez (2020). P is defined as $([1 III]\lambda 4959 + \lambda 5007)/[1 II]\lambda 3727 + [1 III]\lambda 4959 + \lambda 5007$. Green and pink lines represent the theoretical relations derived by Garnett (1992, equation 13) and Pérez-Montero & Contini (2009, equation 14), respectively.

$\lambda 5007$. The following relations, which hold for $0.60 \lesssim t_e(O^{2+}) \lesssim 1.7$, were derived.
For $P < 0.5$,

$$\frac{1}{t_e(N^+)} = \frac{0.54(\pm 0.05)}{t_e(O^{2+})} + 0.52(\pm 0.08), \qquad (11)$$

and for $P > 0.5$,

$$\frac{1}{t_e(N^+)} = \frac{0.61(\pm 0.04)}{t_e(O^{2+})} + 0.36(\pm 0.04). \qquad (12)$$

(iv) Garnett (1992): this author, by using the photoionization model results derived by Stasińska (1982), proposed the relation

$$t_e(S^{2+}) = 0.83 \times t_e(O^{2+}) - 0.17, \qquad (13)$$

valid for $0.4 \lesssim t_e(O^{2+}) \lesssim 1.8$.

(v) Pérez-Montero & Contini (2009): using photoionization model results built through the CLOUDY code these authors deduce a relation between $T_e(O^{2+})$ and $T_e(N^+)$ given by

$$t_e(N^+) = \frac{1.85}{t_e(O^{2+})^{-1} + 0.72}, \qquad (14)$$

with a valid range $0.60 \lesssim t_e(O^{2+}) \lesssim 1.8$.

In Fig. 7, the above relations are compared with our estimates and our own temperature relations. It can be seen in the bottom panel of Fig. 7 that Sy 2 nuclei present similar $T_e(N^+)$ values for a

given $T_e(O^{2+})$ to those from SFs. Otherwise, in Fig. 7, upper panel, $T_e(S^{2+})$ NLR estimates are higher than those in SFs. This result indicates that NLRs have a hotter high-ionization zone than the one in SFs. This is probably due to the known fact that SEDs of AGNs are harder than the ones of SFs. Moreover, gas shocks present in AGNs can produce a very distinct temperature structure than that in SFs, where shocks have a little influence. In fact, Dors et al. (2021) built detailed composite models of photoionization and shock ionization based on the SUMA code (Viegas-Aldrovandi & Contini 1989) to reproduce optical emission lines emitted by NLRs of 244 Sy 2 nuclei. Their models predicted an abrupt increase in temperature near the shock front, reaching values of $\sim 10^5$ K, mainly in shock-dominated objects (see fig. 14 of Dors et al. 2021). In summary, our temperature estimates support the scenario where AGNs have complex spatial distributions of gas temperature and a variety of mechanisms can drive the temperature and ionization (e.g. see Bedregal et al. 2009; Busch et al. 2016; Durré & Mould 2018; Fazeli et al. 2019).

4.2 Sulphur abundances

According to the inside-out scheme, galaxies begin to form stars in their inner regions before the outer ones (e.g. Samland, Hensler & Theis 1997; Portinari & Chiosi 1999; Boissier & Prantzos 2000; Sommer-Larsen, Götz & Portinari 2003; Mollá & Díaz 2005; Nelson et al. 2012, 2016; Vincenzo & Kobayashi 2018) producing radial metallicity gradients with negative slopes (i.e. the metalicity decreases with the increase of the galactocentric distance; e.g. Pilyugin, Vílchez & Contini 2004). Thus, due to the location of AGNs in galactic discs, they are expected to have high abundance of heavy elements; in other words, AGNs with low abundances are barely found in the local universe (e.g. Groves et al. 2006; Izotov & Thuan 2008; Izotov et al. 2010; Kawasaki et al. 2017; Dors et al. 2020a). However, AGNs seem to have a more complex cosmic chemical evolution than SFs. For instance, Matteucci & Padovani (1993), by means of self-consistent models of galaxy evolution, showed that AGNs in galaxies around the lifetime of 10^9 yr ($z \sim 5$) reach an abundance of elements divided into two classes: (i) elements with 2–3 times the solar abundance (C, Ne, O, and Mg) and (ii) the ones with abundances ranging from 5 to 10 times the solar abundance (N, Ni, and Fe). Conversely, low abundance or metallicity have been derived at high redshift from SFs (see Curti et al. 2023 and references therein). Despite the fact that Matteucci & Padovani (1993) did not consider sulphur (an α-element), its abundance would increase similarly to the oxygen abundance, i.e. the expectation will be a constant S/O abundance ratio.

Optical surveys, such as SDSS, have made plenty of AGNs spectroscopic data available, which make the determinations of quantitative sulphur abundance possible in this class of objects. In this sense, we present a detailed analysis of sulphur abundance from our Sy 2 sample and a comparison with some previous results obtained from SFs. In view of that, we consider the following SF estimates that relied on the T_e method.

(i) Hägele et al. (2006): these authors presented calculations for several heavy elements from a sample of H II galaxies (33 objects) and GHRs (34 objects) by using the T_e method. In particular, for the sulphur abundance, they assumed the ICF approach proposed by Barker (1980) with the α exponent equal to 2.5. Following the same procedure, Hägele et al. (2008, 2011, 2012) studied another 11 H II galaxies and knots belonging to this kind of objects that we include in our control sample.

(ii) CHAOS project: the Chemical Abundances Of Spirals (CHAOS;[5] Berg et al. 2015) combines the power of the Large Binocular Telescope (LBT) with the broad spectral range and sensitivity of the Multi-Object Double Spectrograph (MODS) to derive abundances, which relied on the T_e method, for a large sample of H II regions in spiral galaxies. Taking these valuable data into account, we consider abundance estimates for 135 disc H II regions located in NGC 5457, NGC 3184, and NGC 2403 by Croxall et al. (2016), Berg et al. (2020), and Rogers et al. (2021), respectively. These authors adopted the sulphur ICF given by equation (7) for $(O^+/O) \gtrsim 0.6$ and the theoretical ICF from Thuan, Izotov & Lipovetsky (1995) when $(O^+/O) \lesssim 0.6$.

Along this section, we have used the SF abundance estimates from the above authors as benchmark. We emphasize that any selection effect, such as that which may arise as a result of the existence of auroral lines in spectra, will be present in both our AGN sample and the SF sample taken from the literature.

Our sulphur ICFs for the Seyfert galaxies (listed in Table A3) indicate values between ~ 1.1 and ~ 3.0, with an averaged value of 1.44, i.e. about 45 per cent of the sulphur is in higher ionization stages than S^{2+}. We found an ICF value higher than 2.0 for only two objects: 2.02 and 2.94 for Mrk 573 and NGC 7674, respectively. Interestingly, for the most extreme ICF value, i.e. for NGC 7674, Kharb, Lal & Merritt (2017), by using radio long baseline interferometry, hinted that this object hosts a binary supermassive black hole (for a different conclusion see Breiding et al. 2022). Moreover, additional evidence that this object has a hard ionizing spectra is the presence of emission lines of high-ionization ions [Ne V]$\lambda 3346$, $\lambda 3426$, as observed by Kraemer et al. (1994). In any case, even if this object is ruled out from the average ICF calculations, a similar value (1.40) is obtained. In order to compare our sulphur ICF values with those from SFs, we consider the ICFs derived by Hägele et al. (2006) and from the CHAOS project. In the left-hand panel of Fig. 8, the distribution of sulphur ICFs for Sy 2s and SFs is shown, where it can be seen that a good agreement exist among them, even though the GHRs present a distribution peak at lower values. It is worth to be noted that most of the objects (~ 90 per cent) belonging to the distinct object classes present sulphur ICFs lower than ~ 2. The range and average of the ICFs for our sample of Sy 2, H II galaxies, GHRs, and disc H II regions are presented in Table 4 showing that the different samples have similar ICF values. Therefore, despite the fact that Sy 2s have a harder ionizing source than SFs, these two distinct object classes have similar sulphur ionic fractions.

Concerning the total sulphur abundance, in the right-hand panel of Fig. 8, we present the S/H abundance distribution for our sample of Sy 2 nuclei, H II galaxies, and GHRs from Hägele et al. (2006, 2008, 2011, 2012) and for disc H II regions from the CHAOS project. Also in this plot, the sulphur solar abundance $12 + \log(S/H)_\odot = 7.27$ derived by Grevesse & Sauval (1998) is represented by the dashed line. We note that the Sy 2s present an intermediate S/H distribution between that of GHRs and the disc H II regions, while H II galaxies tend to present lower sulphur abundances. In Table 4, the range and S/H average values for our AGN sample and for the SF benchmark sample are listed. The Sy 2s present S/H values in the range of $6.2 < 12 + \log(S/H) < 7.5$ and considering the sulphur solar value as $12 + \log(S/H)_\odot = 7.26$ (Grevesse & Sauval 1998), represents $0.1 < (S/S_\odot) < 1.8$, where most of the objects (40/45) have subsolar sulphur abundance. This

---

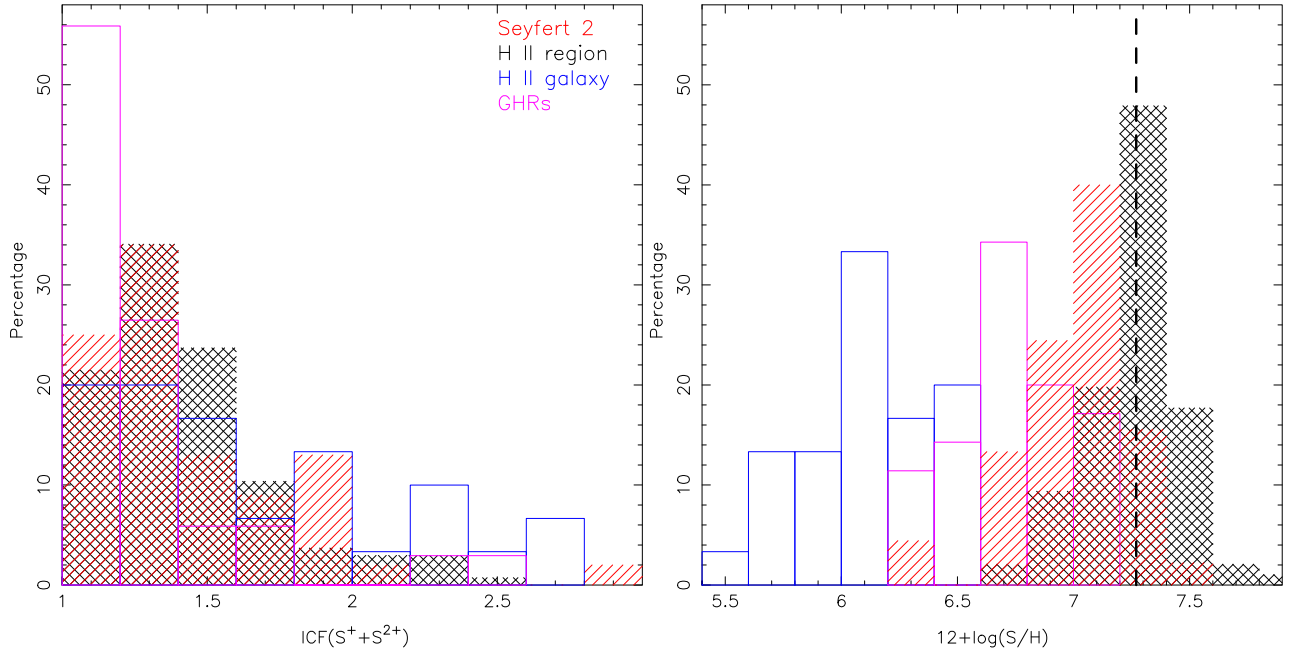[5]https://www.danielleaberg.com/chaos

Figure 8. Left-hand panel: distributions for the sulphur ICF (see Section 3.2.2). Red distribution is derived from our Sy 2 sample by using equation (7) (values listed in Table A3). Black distribution is derived by using values from disc H II region estimates (i.e. results from CHAOS project) assuming equation (7) for $(O^+/O) \gtrsim 0.6$ and the theoretical ICF from Thuan et al. (1995) when $(O^+/O) \lesssim 0.6$. Blue distribution corresponds to H II galaxies values from Hägele et al. (2006, 2008, 2011, 2012) and pink distribution corresponds to GHRs from Hägele et al. (2006), and for both kind of objects the approach proposed by Barker (1980) was used. Right-hand panel: distributions for the sulphur abundance. Dashed line represents the sulphur solar abundance $12 + \log(S/H)_\odot = 7.27$ derived by Grevesse & Sauval (1998). The color code is the same as in left-hand panel.

Table 4. Range and average sulphur ICF, S/H, O/H, and S/O abundance values for our sample of Sy 2s, disc H II regions, H II galaxies, and giant H II regions (GHRs).

Object type	ICF($S^+ + S^{2+}$)		$12 + \log(S/H)$		$12 + \log(O/H)$		$\log(S/O)$		Ref.
	Range	Average	Range	Average	Range	Average	Range	Average	
Sy 2	1.1–3.0	1.44	6.2–7.5	6.98 ± 0.25	8.0–9.1	8.71 ± 0.24	-2.4 to -1.3	-1.64 ± 0.20	1
H II region	1.1–2.5	1.43	6.2–7.9	7.11 ± 0.28	7.8–8.9	8.47 ± 0.19	-1.7 to -0.9	-1.35 ± 0.15	2
H II galaxy	1.0–2.8	1.66	5.5–6.6	6.10 ± 0.27	7.0–8.2	7.79 ± 0.30	-2.0 to -1.4	-1.67 ± 0.15	3, 4
GHR	1.0–2.5	1.26	6.2–7.2	6.73 ± 0.24	7.6–8.6	8.12 ± 0.23	-1.9 to -0.7	-1.38 ± 0.30	4

Note. References: 1 – this work; 2 – Croxall et al. (2016), Berg et al. (2020), and Rogers et al. (2021); 3 – Hägele et al. (2008, 2011, 2012); and 4 – Hägele et al. (2006).

result can be biased due to the fact that we selected only objects that have the [S III]λ9069 and auroral line [O III]λ4363 measured, resulting (see Table 4) only in Sy 2s with O/H values in the range $8.0 \lesssim 12 + \log(O/H) \lesssim 9.1$ or $0.2 \lesssim (Z/Z_\odot) \lesssim 2.6$, adopting the solar oxygen value of $12 + \log(O/H)_\odot = 8.69$ (Allende Prieto et al. 2001). Dors et al. (2020a), who considered a sample of 463 confirmed Seyfert 2 AGNs ($z \lesssim 0.4$) and used distinct methods that did not necessarily required auroral lines, found values in the range $7.1 \lesssim 12 + \log(O/H) \lesssim 9.2$ or $0.02 \lesssim (Z/Z_\odot) \lesssim 3.2$. Therefore, lower and higher S/H abundances would be probably derived in the sample if the data by Dors et al. (2020a) could be taken into account. In any case, the abundance estimates from the CHAOS project comprise inner disc H II regions, therefore, it is expected that these objects and Sy 2 nuclei would have similar S/H abundances, when a large sample of objects is considered. Interestingly, the maximum S/H value ($\sim$7.9 dex) is derived for disc H II regions while sulphur abundances in Sy 2s reach up to $\sim$7.5 dex. This result points to a distinct chemical enrichment of the ISM near the AGNs in comparison to that of the innermost disc H II regions. We emphasize that a more detailed comparison taking into account SFs and AGNs

located in galaxies with similar mass (see do Nascimento et al. 2022) is need to confirm this result.

In Fig. 9, we show a plot of the S/H versus O/H abundances for our Sy 2 sample and for the SF benchmark. Also in this figure, the range of the S/H values derived from the photoionization models by Storchi-Bergmann & Pastoriza (1990) and considering a larger sample of AGNs than our data is indicated. Berg et al. (2020) summarized the radial sulphur gradients (and the gradients for other elements) in four spiral galaxies from the CHAOS project, which are represented by

$$12 + \log(S/H) = \text{grad}(S) \times R + Y_0(S), \quad (15)$$

where grad(S) is the value of the slope of the sulphur gradient, R is the radial galactic distance, and $Y_0(S)$ is the extrapolated value of S/H gradient to the galactic center $R = 0$. The range of $Y_0(S)$ derived by Berg et al. (2020) is also represented in Fig. 9. We note that, for a given O/H value, in general Sy 2s present lower S/H values than the majority of disc H II regions and than those from extrapolated gradients. Again, this discrepancy can be due to the distinct chemical evolution of AGNs and SFs or even due to the small AGN sample (the sample contains only 45 objects).
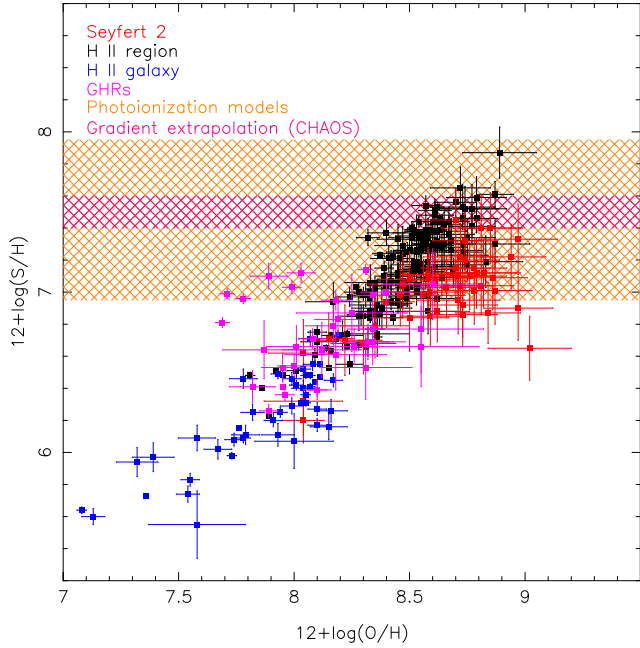
Figure 9. Relation between the total sulphur and oxygen abundances [12+log(S/H) versus $12 + \log(\text{O/H})$]. Red points represent our Sy 2 nuclei direct estimates. Black points represent estimates from disc H II regions also obtained through the T_e method from the CHAOS project. Pink points represent GHRs estimated from Hägele et al. (2006) and blue ones those estimates for H II galaxies from Hägele et al. (2006, 2008, 2011, 2012). The orange hatched area represents the range of S/H values inferred through photoionization models for a sample of 177 Seyfert galaxies by Storchi-Bergmann & Pastoriza (1990). The magenta hatched area represents the range of S/H values obtained from the extrapolation of radial abundance gradients to central parts of four (NGC 0628, NGC 5194, NGC 5457, and NGC 3184) spiral galaxies by Berg et al. (2020).

H II galaxies and GHRs present lower S/H and O/H abundances in comparison with the Sy 2s, which indicate that the former objects are less chemically evolved than the latter. Finally, the model results by Storchi-Bergmann & Pastoriza (1990) predicted, on average, higher (~0.3 dex) S/H values than those derived by using the T_e method for Sy 2s. This discrepancy can be partly due to the known problem of photoionization models overestimating abundances in comparison to the T_e method. In fact, Dors et al. (2020b) showed that direct temperature estimates of $T_e(\text{O}^{2+})$ are higher (up to 11 000 K) than those predicted by photoionization models, which translates into an overestimate of the O/H abundance of up to ~1 dex (with an average value of ~0.2 dex) by the photoionization models. In order to ascertain if the temperature problem also exists in the sulphur temperatures, in Fig. 10, we compare our direct temperature estimates (shown in Fig. 4) with temperature predictions by the photoionization models built with the CLOUDY code by Carvalho et al. (2020) taking into account a wide range of NLR nebular parameters.

(i) Metallicity: $(Z/Z_\odot) = 3.0, 2.0, 1.0, 0.75, 0.5,$ and 0.2.
(ii) Electron density: $N_e \, (\text{cm}^{-3}) = 3000, 1500, 500,$ and 100.
(iii) Ionization parameter (U): $\log U$ ranging from -1.5 to -3.5, with step of 0.5 dex.
(iv) Spectra energy distribution (SED): the SED is parametrized by the continuum between 2 keV and 2500 Å (Tananbaum et al. 1979) and it is described by a power law with a spectral index $\alpha_{\text{ox}} = -0.8$, -1.1, and -1.4.
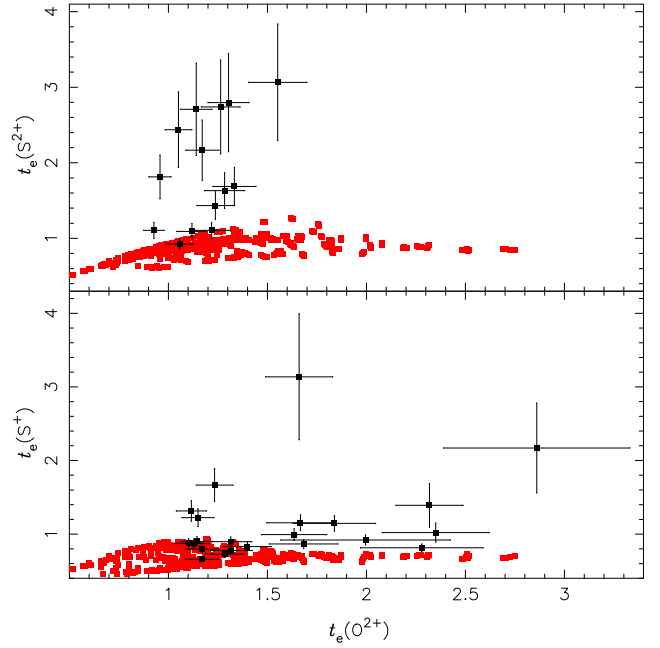

Figure 10. Temperatures (in units of 10^4 K) for the S^+ (bottom panel) and S^{2+} (upper panel) versus the temperature for O^{2+}. Black points are Sy 2 direct estimations that relied on auroral lines (see Section 4.1). Red points are temperature predictions by AGN photoionization models built with the CLOUDY code by Carvalho et al. (2020).

In Fig. 10, it can be seen that similar to oxygen temperatures (see Dors et al. 2020b) direct temperature estimates for S^+ and S^{2+} are higher than those predicted by AGN photoioinization models.[6] Thus, this result explains the discrepancy between the sulphur abundance inferred by the photoionization models built by Storchi-Bergmann & Pastoriza (1990) and those calculated from our sample by using the T_e method.

Finally, in Fig. 11, we show a plot of log(S/O) versus $12 + \log(\text{O/H})$, which compares our direct abundance estimates with the SF benchmark. Considering the estimates of all objects (AGN + SF), we provide the following relation:

$$\log(\text{S/O}) = +0.06(\pm 0.03) \times [12 + \log(\text{O/H})] - 1.94(\pm 0.33), \quad (16)$$

with the Pearson coefficient parameters ($R = 0.09 \pm 0.07$ and p-value $= 0.24$), i.e. there is no correlation between the estimations. Thus, our estimates combined with those from a large sample of SFs suggest that S/O is constant over a wide range of O/H, as found by recent results from the CHAOS project (see Rogers et al. 2021 and references therein). However, in Fig. 11, it can be seen that there is a clear trend of S/O values of Sy 2 decreasing with O/H in the high-metallicity regime. The same behaviour was found from H II regions, for instance, by Dors et al. (2016) and Díaz & Zamora (2022).

It is worth to mention that emission lines of AGNs, such as [S III]λ9069, λ9532 and auroral lines (mainly [N II]λ5755 and [S III]λ6312), are either measured with low S/N (~2) or unavailable in the literature (e.g. see Koski 1978; Dopita et al. 2015). This implies that chemical abundance studies of AGNs are difficult to be carried out and, even when it is possible to determine the abundance directly, higher (a factor of ~2, see Fig. 9) abun-

---

[6]Model temperatures values in Fig. 10 correspond to the mean temperature for S^+ and S^{2+} over the nebular AGN radius times the electron density.
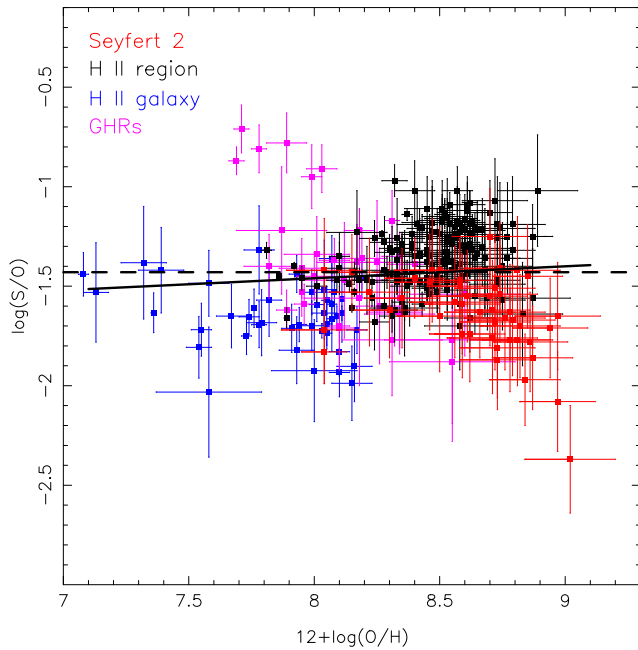
Figure 11. Relation between log(S/O) and 12 + log(O/H). Red points represent our Sy 2 nuclei direct estimates. Pink points represent direct estimates for GHRs from Hägele et al. (2006). Black points represent estimates from disc H II regions obtained also through T_e method by Berg et al. (2020). Blue points represent direct estimates for H II galaxies by Hägele et al. (2006, 2008, 2011, 2012). Dashed line represents the solar value of log(S/O)$_\odot$ = −1.43 (Grevesse & Sauval 1998; Allende Prieto et al. 2001). Solid line represents the linear regression considering all the estimates given by equation (16).

dance errors in comparison with those of SFs are derived. The next generation of telescopes, such as the Giant Magellan Telescope, European Extremely Large Telescope, and Thirty Meter Telescope, will provide higher S/N measurements of weak AGN emission lines and will allow a breakthrough in our understanding of the chemical abundance in AGNs and objects with very high metallicity.

5 CONCLUSIONS

We have used observations of the intensities of narrow emission lines in the spectral interval $3000 < \lambda(\text{Å}) < 9100$ of sample of 45 nearby ($z \lesssim 0.08$) Seyfert 2 nuclei taken from SDSS DR17 and other compilations from the literature to perform direct estimations of electron temperatures through the T_e method and estimates of sulphur and oxygen abundances relative to hydrogen. These estimates were compared with those from local SFs, i.e. disc H II regions, H II galaxies, and GHRs, whose abundance estimates were compiled from the literature. Regarding the electron temperatures, we found that Seyfert 2 and SFs have similar temperature in the gas regions where most S^+ is located. However, this result is not derived for the zones where most S^{2+} is located: S^{2+} electron temperatures are higher ($\sim 10\,000$ K) from Seyfert 2 than from SFs. We interpret this result as, probably, due to the known feature of SEDs of AGNs are harder than that of SFs, producing a hotter gas in the innermost narrow line region of AGNs. For our sample of Seyfert 2, we derived total sulphur abundances in the range of $6.2 \lesssim 12 + \log(\text{S/H}) \lesssim 7.5$ or $0.1 \lesssim (\text{S/S}_\odot) \lesssim 1.8$. The Seyfert 2 sulphur abundances are lower by a factor of ~ 0.4 dex than those derived for SFs with similar

metallicities. This discrepancy can be interpreted as due to a distinct chemical enrichment of the ISM near the AGNs in comparison to that of the SFs. The relation between S/O and O/H abundance ratios derived from our Seyfert 2 nuclei sample presents an abrupt (~ 0.5 dex) decrease with the increase of O/H for the high-metallicity regime $[12 + \log(\text{O/H}) \gtrsim 8.7)]$, which is not derived from SFs. However, when our Sy 2 estimates are combined with those from a large sample of SFs, we did not find any dependence between S/O and O/H, supporting the idea that sulphur and oxygen are produced by stars with similar mass range and that the IMF is universal.

DATA AVAILABILITY

The data underlying this paper will be shared on reasonable request to the corresponding author.

REFERENCES

Abazajian K. et al., 2005, AJ, 129, 1755
Abazajian K. N. et al., 2009, ApJS, 182, 543
Abdurro'uf et al., 2022, ApJS, 259, 35
Aihara H. et al., 2011, ApJS, 193, 29
Aldrovandi S. M. V., Contini M., 1984, A&A, 140, 368

Allende Prieto C., Barklem P. S., Lambert D. L., Cunha K., 2004, A&A, 420, 183

Allende Prieto C., Lambert D. L., Asplund M., 2001, ApJ, 556, L63

Aller L. H., Czyzak S. J., 1983, ApJS, 51, 211

Alloin D., Bica E., Bonatto C., Prugniel P., 1992, A&A, 266, 117

Arellano-Córdova K. Z. et al., 2022, ApJ, 935, 74

Arellano-Córdova K. Z., Esteban C., García-Rojas J., Méndez-Delgado J. E., 2020, MNRAS, 496, 1051

Arellano-Córdova K. Z., Rodríguez M., 2020, MNRAS, 497, 672

Armah M. et al., 2021, MNRAS, 508, 371

Armus L. et al., 2023, ApJ, 942, L37

Barker T., 1980, ApJ, 240, 99

Bedregal A. G., Colina L., Alonso-Herrero A., Arribas S., 2009, ApJ, 698, 1852

Berg D. A., Pogge R. W., Skillman E. D., Croxall K. V., Moustakas J., Rogers N. S. J., Sun J., 2020, ApJ, 893, 96

Berg D. A., Skillman E. D., Croxall K. V., Pogge R. W., Moustakas J., Johnson-Groh M., 2015, ApJ, 806, 16

Berg D. A., Skillman E. D., Garnett D. R., Croxall K. V., Marble A. R., Smith J. D., Gordon K., Kennicutt Robert C. J., 2013, ApJ, 775, 128

Bergvall N., Johansson L., Olofsson K., 1986, A&A, 166, 92

Bernard-Salas J., Pottasch S. R., Gutenkunst S., Morris P. W., Houck J. R., 2008, ApJ, 672, 274

Bianchi S., Chiaberge M., Evans D. A., Guainazzi M., Baldi R. D., Matt G., Piconcelli E., 2010, MNRAS, 405, 553

Binette L., Matadamas R., Hägele G. F., Nicholls D. C., Magris C. G., Peña-Guerrero M. Á., Morisset C., Rodríguez-González A., 2012, A&A, 547, A29

Bogdán Á., Kraft R. P., Evans D. A., Andrade-Santos F., Forman W. R., 2017, ApJ, 848, 61

Boissier S., Prantzos N., 2000, MNRAS, 312, 398

Bonifacio P., Caffau E., Centurión M., Molaro P., Vladilo G., 2001, MNRAS, 325, 767

Breiding P., Burke-Spolaor S., An T., Bansal K., Mohan P., Taylor G. B., Zhang Y., 2022, ApJ, 933, 143

Busch G. et al., 2016, A&A, 587, A138

Caffau E., Bonifacio P., Faraggiana R., François P., Gratton R. G., Barbieri M., 2005, A&A, 441, 533

Cardaci M. V., Santos-Lleó M., Hägele G. F., Krongold Y., Díaz A. I., Rodríguez-Pascual P., 2011, A&A, 530, A125

Cardaci M. V., Santos-Lleó M., Krongold Y., Hägele G. F., Díaz A. I., Rodríguez-Pascual P., 2009, A&A, 505, 541

Cardelli J. A., Clayton G. C., Mathis J. S., 1989, ApJ, 345, 245

Carvalho S. P. et al., 2020, MNRAS, 492, 5675

Castro C. S., Dors O. L., Cardaci M. V., Hägele G. F., 2017, MNRAS, 467, 1507

Cavichia O., Costa R. D. D., Maciel W. J., Mollá M., 2017, MNRAS, 468, 272

Centurión M., Bonifacio P., Molaro P., Vladilo G., 2000, ApJ, 536, 540

Cerqueira-Campos F. C., Rodríguez-Ardila A., Riffel R., Marinello M., Prieto A., Dahmer-Hahn L. G., 2021, MNRAS, 500, 2666

Chevallard J., Charlot S., 2016, MNRAS, 462, 1415

Christensen T., Petersen L., Gammelgaard P., 1997, A&A, 322, 41

Cid Fernandes R., Mateus A., Sodré L., Stasińska G., Gomes J. M., 2005, MNRAS, 358, 363

Cid Fernandes R., Stasińska G., Schlickmann M. S., Mateus A., Vale Asari N., Schoenell W., Sodré L., 2010, MNRAS, 403, 1036

Cohen R. D., 1983, ApJ, 273, 489

Congiu E. et al., 2017, MNRAS, 471, 562

Costa R. D. D., Uchida M. M. M., Maciel W. J., 2004, A&A, 423, 199

Costa Silva A. R., Delgado Mena E., Tsantaki M., 2020, A&A, 634, A136

Croxall K. V., Pogge R. W., Berg D. A., Skillman E. D., Moustakas J., 2015, ApJ, 808, 42

Croxall K. V., Pogge R. W., Berg D. A., Skillman E. D., Moustakas J., 2016, ApJ, 830, 4

Curti M. et al., 2023, MNRAS, 518, 425

Danehkar A., Oey M. S., Gray W. J., 2022, ApJ, 937, 68

Davies R. L., Rich J. A., Kewley L. J., Dopita M. A., 2014, MNRAS, 439, 3835

Delgado-Inglada G., Morisset C., Stasińska G., 2014, MNRAS, 440, 536

Denicoló G., Terlevich R., Terlevich E., 2002, MNRAS, 330, 69

Diamond-Stanic A. M., Rieke G. H., 2012, ApJ, 746, 168

Díaz Á. I., Terlevich E., Castellanos M., Hägele G. F., 2007, MNRAS, 382, 251

Díaz A. I., Terlevich E., Vilchez J. M., Pagel B. E. J., Edmunds M. G., 1991, MNRAS, 253, 245

Díaz Á. I., Zamora S., 2022, MNRAS, 511, 4377

do Nascimento J. C. et al., 2022, MNRAS, 513, 807

Dopita M. A. et al., 2005, ApJ, 619, 755

Dopita M. A. et al., 2015, ApJS, 217, 12

Dopita M. A., Sutherland R. S., 1995, ApJ, 455, 468

Dors O. L. et al., 2020a, MNRAS, 492, 468

Dors O. L. et al., 2022, MNRAS, 514, 5506

Dors O. L. J., Arellano-Córdova K. Z., Cardaci M. V., Hägele G. F., 2017, MNRAS, 468, L113

Dors O. L. J., Storchi-Bergmann T., Riffel R. A., Schimdt A. A., 2008, A&A, 482, 59

Dors O. L., Agarwal B., Hägele G. F., Cardaci M. V., Rydberg C.-E., Riffel R. A., Oliveira A. S., Krabbe A. C., 2018, MNRAS, 479, 2294

Dors O. L., Cardaci M. V., Hägele G. F., Krabbe Â. C., 2014, MNRAS, 443, 1291

Dors O. L., Contini M., Riffel R. A., Pérez-Montero E., Krabbe A. C., Cardaci M. V., Hägele G. F., 2021, MNRAS, 501, 1370

Dors O. L., Maiolino R., Cardaci M. V., Hägele G. F., Krabbe A. C., Pérez-Montero E., Armah M., 2020b, MNRAS, 496, 3209

Dors O. L., Monteiro A. F., Cardaci M. V., Hägele G. F., Krabbe A. C., 2019, MNRAS, 486, 5853

Dors O. L., Pérez-Montero E., Hägele G. F., Cardaci M. V., Krabbe A. C., 2016, MNRAS, 456, 4407

Durré M., Mould J., 2018, ApJ, 867, 149

Espíritu J. N., Peimbert A., 2021, MNRAS, 508, 2668

Fang X. et al., 2018, ApJ, 853, 50

Fathivavsari H., Petitjean P., Ledoux C., Noterdaeme P., Srianand R., Rahmani H., Ajabshirizadeh A., 2013, MNRAS, 435, 1727

Fazeli N., Busch G., Valencia-S. M., Eckart A., Zajaček M., Combes F., García-Burillo S., 2019, A&A, 622, A128

Feltre A., Charlot S., Gutkin J., 2016, MNRAS, 456, 3354

Ferland G. J. et al., 2013, Rev. Mex. Astron. Astrofis., 49, 137

Ferland G. J., Osterbrock D. E., 1986, ApJ, 300, 658

Fernández V., Terlevich E., Díaz A. I., Terlevich R., 2019, MNRAS, 487, 3221

Fernández-Ontiveros J. A., Spinoglio L., Pereira-Santaella M., Malkan M. A., Andreani P., Dasyra K. M., 2016, ApJS, 226, 19

Flury S. R., Moran E. C., 2020, MNRAS, 496, 2191

Fox A., Richter P., Fechner C., 2014, A&A, 572, A102

Freitas I. C. et al., 2018, MNRAS, 476, 2760

Froese Fischer C., Tachiev G., 2004, At. Data Nucl. Data Tables, 87, 1

Froese Fischer C., Tachiev G., Irimia A., 2006, At. Data Nucl. Data Tables, 92, 607

Gaia Collaboration et al., 2022, A&A, preprint (arXiv:2206.05534)

García-Benito R. et al., 2010, MNRAS, 408, 2234

García-Burillo S. et al., 2014, A&A, 567, A125

García-Rojas J., Morisset C., Jones D., Wesson R., Boffin H. M. J., Monteiro H., Corradi R. L. M., Rodríguez-Gil P., 2022, MNRAS, 510, 5444

Garnett D. R., 1989, ApJ, 345, 282

Garnett D. R., 1992, AJ, 103, 1330

Garnett D. R., Shields G. A., Skillman E. D., Sagan S. P., Dufour R. J., 1997, ApJ, 489, 63

Goodrich R. W., Osterbrock D. E., 1983, ApJ, 269, 416

Grevesse N., Sauval A. J., 1998, Space Sci. Rev., 85, 161

Gronow S., Côté B., Lach F., Seitenzahl I. R., Collins C. E., Sim S. A., Röpke F. K., 2021, A&A, 656, A94

Groves B. A., Heckman T. M., Kauffmann G., 2006, MNRAS, 371, 1559

Guo Y. et al., 2020, ApJ, 898, 26

Guseva N. G., Izotov Y. I., Stasińska G., Fricke K. J., Henkel C., Papaderos P., 2011, A&A, 529, A149

Hägele G. F., Díaz Á. I., Terlevich E., Terlevich R., Pérez-Montero E., Cardaci M. V., 2008, MNRAS, 383, 209

Hägele G. F., Firpo V., Bosch G., Díaz Á. I., Morrell N., 2012, MNRAS, 422, 3475

Hägele G. F., García-Benito R., Pérez-Montero E., Díaz Á. I., Cardaci M. V., Firpo V., Terlevich E., Terlevich R., 2011, MNRAS, 414, 272

Hägele G. F., Pérez-Montero E., Díaz Á. I., Terlevich E., Terlevich R., 2006, MNRAS, 372, 293

Henry R. B. C., Kwitter K. B., Balick B., 2004, AJ, 127, 2284

Hummer D. G., Storey P. J., 1987, MNRAS, 224, 801

Israelian G., Rebolo R., 2001, ApJ, 557, L43

Izotov Y. I., Guseva N. G., Fricke K. J., Stasińska G., Henkel C., Papaderos P., 2010, A&A, 517, A90

Izotov Y. I., Stasińska G., Meynet G., Guseva N. G., Thuan T. X., 2006, A&A, 448, 955

Izotov Y. I., Thuan T. X., 2008, ApJ, 687, 133

Jenkins E. B., 2009, ApJ, 700, 1299

Jin Y., Kewley L. J., Sutherland R., 2022, ApJ, 927, 37

Kakkad D. et al., 2018, A&A, 618, A6

Kawasaki K., Nagao T., Toba Y., Terao K., Matsuoka K., 2017, ApJ, 842, 44

Kennicutt Robert C. J., Bresolin F., Garnett D. R., 2003, ApJ, 591, 801

Kewley L. J., Dopita M. A., Sutherland R. S., Heisler C. A., Trevena J., 2001, ApJ, 556, 121

Kewley L. J., Jansen R. A., Geller M. J., 2005, PASP, 117, 227

Kewley L. J., Nicholls D. C., Sutherland R. S., 2019, ARA&A, 57, 511

Kharb P., Lal D. V., Merritt D., 2017, Nat. Astron., 1, 727

Kisielius R., Storey P. J., Ferland G. J., Keenan F. P., 2009, MNRAS, 397, 903

Koski A. T., 1978, ApJ, 223, 56

Kraemer S. B., Turner T. J., Couto J. D., Crenshaw D. M., Schmitt H. R., Revalski M., Fischer T. C., 2020, MNRAS, 493, 3893

Kraemer S. B., Wu C.-C., Crenshaw D. M., Harrington J. P., 1994, ApJ, 435, 171

López-Sánchez A. R., Esteban C., 2009, A&A, 508, 615

Lucertini F., Monaco L., Caffau E., Bonifacio P., Mucciarelli A., 2022, A&A, 657, A29

Luridiana V., Morisset C., Shaw R. A., 2015, A&A, 573, A42

Maiolino R., Mannucci F., 2019, A&AR, 27, 3

Maksym W. P. et al., 2019, ApJ, 872, 94

Malkan M. A., Oke J. B., 1983, ApJ, 265, 92

Mannucci F. et al., 2021, MNRAS, 508, 1582

Mateus A., Sodré L., Cid Fernandes R., Stasińska G., Schoenell W., Gomes J. M., 2006, MNRAS, 370, 721

Matsuoka K., Nagao T., Maiolino R., Marconi A., Taniguchi Y., 2009, A&A, 503, 721

Matsuoka K., Nagao T., Marconi A., Maiolino R., Mannucci F., Cresci G., Terao K., Ikeda H., 2018, A&A, 616, L4

Matteucci F., Padovani P., 1993, ApJ, 419, 485

Mignoli M. et al., 2019, A&A, 626, A9

Milingo J. B., Kwitter K. B., Henry R. B. C., Souza S. P., 2010, ApJ, 711, 619

Mingozzi M. et al., 2019, A&A, 622, A146

Mollá M., Díaz A. I., 2005, MNRAS, 358, 521

Monreal-Ibero A., Walsh J. R., Vílchez J. M., 2012, A&A, 544, A60

Monteiro A. F., Dors O. L., 2021, MNRAS, 508, 3023

Nagao T., Maiolino R., Marconi A., 2006, A&A, 459, 85

Nakajima K. et al., 2018, A&A, 612, A94

Nelson E. J. et al., 2012, ApJ, 747, L28

Nelson E. J. et al., 2016, ApJ, 828, 27

Nissen P. E., Akerman C., Asplund M., Fabbian D., Kerber F., Kaufl H. U., Pettini M., 2007, A&A, 469, 319

Nissen P. E., Chen Y. Q., Asplund M., Pettini M., 2004, A&A, 415, 993

Nomoto K., Kobayashi C., Tominaga N., 2013, ARA&A, 51, 457

Osterbrock D. E., 1989, Astrophysics of Gaseous Nebulae and Active Galactic Nuclei. University Science Books, Mill Valley, CA

Pagel B. E. J., 1978, MNRAS, 183, 1P

Pagomenos G. J. S., Bernard-Salas J., Pottasch S. R., 2018, A&A, 615, A29

Peimbert M., Costero R., 1969, Bol. Obser. Tonantzintla Tacubaya, 5, 3

Peimbert M., Peimbert A., Delgado-Inglada G., 2017, PASP, 129, 082001

Perdigon J., de Laverny P., Recio-Blanco A., Fernandez-Alvar E., Santos-Peral P., Kordopatis G., Álvarez M. A., 2021, A&A, 647, A162

Pérez-Díaz B., Masegosa J., Márquez I., Pérez-Montero E., 2021, MNRAS, 505, 4289

Pérez-Montero E. et al., 2011, A&A, 532, A141

Pérez-Montero E., 2017, PASP, 129, 043001

Pérez-Montero E., Contini T., 2009, MNRAS, 398, 949

Pérez-Montero E., Díaz A. I., 2003, MNRAS, 346, 105

Pérez-Montero E., Díaz A. I., Vílchez J. M., Kehrig C., 2006, A&A, 449, 193

Pérez-Montero E., Dors O. L., Vílchez J. M., García-Benito R., Cardaci M. V., Hägele G. F., 2019, MNRAS, 489, 2652

Pettini M., Smith L. J., King D. L., Hunstead R. W., 1997, ApJ, 486, 665

Phillips M. M., Charles P. A., Baldwin J. A., 1983, ApJ, 266, 485

Pilyugin L. S., 2003, A&A, 399, 1003

Pilyugin L. S., Lara-Lopez M. A., Vilchez J. M., Duarte Puertas S., Zinchenko I. A., Dors O. L., 2022, A&A, 668, A5

Pilyugin L. S., Vílchez J. M., Contini T., 2004, A&A, 425, 849

Portinari L., Chiosi C., 1999, A&A, 350, 827

Prochaska J. X., Wolfe A. M., 2002, ApJ, 566, 68

Ramos Almeida C., Pérez García A. M., Acosta-Pulido J. A., Rodríguez Espinosa J. M., Barrena R., Manchado A., 2006, ApJ, 645, 148

Recio-Blanco A. et al., 2022, A&A, preprint(arXiv:2206.05541)

Revalski M. et al., 2018b, ApJ, 867, 88

Revalski M. et al., 2021, ApJ, 910, 139

Revalski M. et al., 2022, ApJ, 930, 14

Revalski M., Crenshaw D. M., Kraemer S. B., Fischer T. C., Schmitt H. R., Machuca C., 2018a, ApJ, 856, 46

Richardson C. T., Allen J. T., Baldwin J. A., Hewett P. C., Ferland G. J., 2014, MNRAS, 437, 2376

Riffel R. A. et al., 2021a, MNRAS, 501, L54

Riffel R. A., Dors O. L., Krabbe A. C., Esteban C., 2021c, MNRAS, 506, L11

Riffel R. A., Storchi-Bergmann T., Zakamska N. L., Riffel R., 2020, MNRAS, 496, 4857

Riffel R. et al., 2021b, MNRAS, 501, 4064

Riffel R., Rodríguez-Ardila A., Pastoriza M. G., 2006, A&A, 457, 61

Ritter C., Herwig F., Jones S., Pignatari M., Fryer C., Hirschi R., 2018, MNRAS, 480, 538

Rodríguez-Ardila A., Prieto M. A., Portilla J. G., Tejeiro J. M., 2011, ApJ, 743, 100

Rogers N. S. J., Skillman E. D., Pogge R. W., Berg D. A., Croxall K. V., Bartlett J., Arellano-Córdova K. Z., Moustakas J., 2022, ApJ, 939, 44

Rogers N. S. J., Skillman E. D., Pogge R. W., Berg D. A., Moustakas J., Croxall K. V., Sun J., 2021, ApJ, 915, 21

Roman-Duval J. et al., 2022, ApJ, 935, 105

Ruschel-Dutra D. et al., 2021, MNRAS, 507, 74

Ruschel-Dutra D., Dall'Agnol De Oliveira B., 2020, danielrd6/ifscube v1.0 (v1.0). Zenodo. Available at: https://doi.org/10.5281/zenodo.3945237

Samland M., Hensler G., Theis C., 1997, ApJ, 476, 544

Savage B. D., Sembach K. R., 1996, ARA&A, 34, 279

Shields G. A., Searle L., 1978, ApJ, 222, 821

Shuder J. M., 1980, ApJ, 240, 32

Shuder J. M., Osterbrock D. E., 1981, ApJ, 250, 55

Sommer-Larsen J., Götz M., Portinari L., 2003, ApJ, 596, 47

Stasińska G., 1982, A&AS, 48, 299

Stasińska G., 1984, A&A, 135, 341

Stasińska G., 1990, A&AS, 83, 501

Storchi-Bergmann T., Pastoriza M. G., 1990, PASP, 102, 1359

Storchi-Bergmann T., Schmitt H. R., Calzetti D., Kinney A. L., 1998, AJ, 115, 909

Storey P. J., Sochi T., Badnell N. R., 2014, MNRAS, 441, 3028

Storey P. J., Zeippen C. J., 2000, MNRAS, 312, 813

Takada-Hidai M. et al., 2002, ApJ, 573, 614

Tananbaum H. et al., 1979, ApJ, 234, L9

Tayal S. S., Gupta G. P., 1999, ApJ, 526, 544

Tayal S. S., Zatsarinny O., 2010, ApJS, 188, 32

Thomas A. D. et al., 2017, ApJS, 232, 11

Thomas A. D., Kewley L. J., Dopita M. A., Groves B. A., Hopkins A. M., Sutherland R. S., 2019, ApJ, 874, 100

Thuan T. X., Izotov Y. I., Lipovetsky V. A., 1995, ApJ, 445, 108

Toribio San Cipriano L., Domínguez-Guzmán G., Esteban C., García-Rojas J., Mesa-Delgado A., Bresolin F., Rodríguez M., Simón-Díaz S., 2017, MNRAS, 467, 3759

Torres-Peimbert S., Peimbert M., 1977, Rev. Mex. Astron. Astrofis., 2, 181

Vale Asari N., Stasińska G., Morisset C., Cid Fernandes R., 2016, MNRAS,

APPENDIX: TABLES

van Zee L., Salzer J. J., Haynes M. P., O'Donoghue A. A., Balonek T. J., 1998, AJ, 116, 2805

Vaona L., Ciroi S., Di Mille F., Cracco V., La Mura G., Rafanelli P., 2012, MNRAS, 427, 1266

Vermeij R., van der Hulst J. M., 2002, A&A, 391, 1081

Vidal-García A., Plat A., Curtis-Lake E., Feltre A., Hirschmann M., Chevallard J., Charlot S., 2022, preprint (arXiv:2211.13648)

Viegas-Aldrovandi S. M., Contini M., 1989, ApJ, 339, 689

Vilchez J. M., Pagel B. E. J., Diaz A. I., Terlevich E., Edmunds M. G., 1988, MNRAS, 235, 633

Vincenzo F., Kobayashi C., 2018, MNRAS, 478, 155

Walsh J. R. et al., 2018, A&A, 620, A169

Wiese W. L., Fuhr J. R., Deters T. M., 1996, Atomic Transition Probabilities of Carbon, Nitrogen, and Oxygen: A Critical Data Compilation. American Chemical Society, Washington, DC

Woosley S. E., Weaver T. A., 1995, ApJS, 101, 181

Xu X., Arav N., Miller T., Korista K. T., Benn C., 2021, MNRAS, 506, 2725

York D. G. et al., 2000, AJ, 120, 1579

Zurita A., Bresolin F., 2012, MNRAS, 427, 1463

Table A1. Emission-line intensities of Seyfert 2s relative to Hβ = 1.00 taken from SDSS DR17 and compiled from the literature. For Mrk 3 the sum [S II]λ6717 + 6731 (in relation to Hβ) is listed. Last column lists the references for the optical and near-infrared lines, except for Mrk 3 and ESO 138 G1 that the line set was taken from only one work.

Object	[O II]λ3727	[O III]λ4363	[O III]λ5007	[N II]λ5755	[S III]λ6312	Hαλ6563	[N II]λ6584	[S II]λ6716	[S II]λ6731	[S III]λ9069 + λ9532	Ref.
Mrk 573	2.13 ± 0.05	0.14 ± 0.011	10.26 ± 0.05	–	–	2.86 ± 0.05	2.34 ± 0.04	0.79 ± 0.01	0.73 ± 0.02	2.58	1, 12[a]
NGC 5728	2.32 ± 0.03	0.11 ± 0.016	9.10 ± 0.11	–	–	2.86 ± 0.13	2.86 ± 0.13	0.97 ± 0.06	0.66 ± 0.03	1.92	1, 12[a]
ESO 428 G14	2.22	0.24	11.2	–	–	2.90	3.13	0.83	0.88	1.87	2, 12[a]
NGC 4388	2.73	0.16	10.55	–	–	2.84	1.50	0.72	0.62	1.10	3, 13[a]
Mrk 78	4.96	0.14	11.94	–	–	2.46	2.46	0.68	0.61	0.89	4, 14[a]
NGC 7674	1.29	0.12	12.55	–	–	3.70	3.68	0.54	0.64	3.15	5, 12[a]
NGC 2110	4.38	0.17	4.76	–	–	2.66	3.76	1.52	1.42	1.91	6, 12[a]
NGC 7682	2.85	0.16	9.34	–	–	3.10	3.03	1.09	1.17	1.95	7, 12[a]
NGC 3227	3.22	0.50	10.73	–	–	2.86	5.01	1.24	1.26	1.66	8, 12[b]
Mrk 1066	3.34	0.08	3.84	–	–	2.76	2.42	0.51	0.55	0.75	9, 12[a]
Mrk 3[b,c]	4.84	0.23	11.22	–	–	2.85	3.21	1.45		2.59	10
ESO 138 G1[c]	2.35 ± 0.05	0.34 ± 0.02	8.71 ± 0.25	–	–	3.01 ± 0.10	0.68 ± 0.03	0.47 ± 0.03	0.48 ± 0.03	0.69	11
55978−0990	6.76 ± 0.43	0.14 ± 0.06	10.70 ± 0.73	–	–	2.86 ± 0.31	3.30 ± 0.36	1.07 ± 0.18	0.87 ± 0.16	2.06 ± 0.66	15
56104−0966	6.31 ± 0.14	0.07 ± 0.02	8.51 ± 0.20	–	–	2.86 ± 0.09	1.04 ± 0.04	0.62 ± 0.03	0.56 ± 0.03	0.73 ± 0.12	15
55181−0154	4.12 ± 0.31	0.06 ± 0.03	7.82 ± 0.28	–	0.15 ± 0.04	2.86 ± 0.21	2.05 ± 0.15	0.60 ± 0.06	0.61 ± 0.06	2.02 ± 0.42	15
56088−0473	2.07 ± 0.01	0.06 ± 0.01	7.70 ± 0.04	–	0.01 ± 0.01	2.86 ± 0.01	0.15 ± 0.01	0.12 ± 0.01	0.11 ± 0.01	0.63 ± 0.02	15
56034−0154	3.02 ± 0.32	0.14 ± 0.01	11.88 ± 0.23	–	0.05 ± 0.03	2.86 ± 0.07	2.13 ± 0.05	0.88 ± 0.03	0.81 ± 0.03	2.10 ± 0.14	15
56067−0382	5.51 ± 1.33	0.21 ± 0.10	8.70 ± 0.83	0.192 ± 0.165	–	2.86 ± 0.52	2.36 ± 0.44	0.86 ± 0.22	0.81 ± 0.22	1.19 ± 0.89	15
56240−0340	8.32 ± 0.52	0.16 ± 0.06	7.24 ± 0.56	0.078 ± 0.047	–	2.86 ± 0.28	2.60 ± 0.26	1.10 ± 0.21	0.86 ± 0.20	3.04 ± 0.94	15
55539−0167	2.79 ± 0.20	0.05 ± 0.02	4.11 ± 0.08	–	–	2.86 ± 0.08	1.91 ± 0.05	0.61 ± 0.03	0.54 ± 0.03	1.08 ± 0.14	15
56626−0636	3.82 ± 0.09	0.06 ± 0.01	6.12 ± 0.10	–	0.10 ± 0.02	2.86 ± 0.07	2.23 ± 0.05	1.06 ± 0.03	0.98 ± 0.03	1.22 ± 0.10	15
56074−0045	4.23 ± 0.32	0.03 ± 0.01	2.69 ± 0.04	–	–	2.86 ± 0.07	1.52 ± 0.04	0.77 ± 0.02	0.58 ± 0.02	0.91 ± 0.11	15
55212−0380	3.52 ± 1.13	0.10 ± 0.03	12.54 ± 0.51	–	–	2.86 ± 0.15	2.94 ± 0.15	0.85 ± 0.06	0.84 ± 0.06	2.41 ± 0.30	15
56399−0302	5.01 ± 0.37	0.08 ± 0.04	3.07 ± 0.19	–	–	2.86 ± 0.23	2.16 ± 0.19	1.58 ± 0.16	1.14 ± 0.14	1.33 ± 0.63	15
56001−0293	5.05 ± 0.20	0.07 ± 0.01	7.63 ± 0.20	0.047 ± 0.037	–	2.86 ± 0.13	1.74 ± 0.08	0.85 ± 0.05	0.61 ± 0.04	1.54 ± 0.21	15
55651−0052	3.28 ± 0.76	0.02 ± 0.01	3.54 ± 0.04	–	0.05 ± 0.01	2.86 ± 0.06	2.06 ± 0.04	0.72 ± 0.02	0.68 ± 0.02	0.94 ± 0.08	15
56566−0794	6.58 ± 0.61	0.05 ± 0.02	4.74 ± 0.12	0.017 ± 0.016	0.08 ± 0.03	2.86 ± 0.10	2.16 ± 0.08	1.26 ± 0.06	1.07 ± 0.05	1.22 ± 0.16	15
56748−0336	4.97 ± 0.51	0.08 ± 0.05	7.11 ± 0.41	–	–	2.86 ± 0.24	3.23 ± 0.27	0.99 ± 0.12	0.89 ± 0.12	1.85 ± 0.50	15
56206−0454	7.35 ± 0.27	0.09 ± 0.02	6.67 ± 0.19	–	0.05 ± 0.03	2.86 ± 0.11	1.21 ± 0.06	1.12 ± 0.05	0.91 ± 0.05	1.08 ± 0.19	15
55860−0112	5.74 ± 1.44	0.11 ± 0.07	7.82 ± 0.66	–	0.15 ± 0.12	2.86 ± 0.33	5.38 ± 0.61	1.80 ± 0.23	1.77 ± 0.23	1.78 ± 0.46	15
56453−0144	3.19 ± 0.37	0.06 ± 0.02	6.42 ± 0.18	–	–	2.86 ± 0.10	2.64 ± 0.10	0.89 ± 0.06	0.78 ± 0.06	2.20 ± 0.31	15
55710−0116	2.72 ± 1.05	0.07 ± 0.02	7.54 ± 0.24	–	0.06 ± 0.04	2.86 ± 0.12	4.47 ± 0.18	1.04 ± 0.06	1.13 ± 0.07	2.58 ± 0.21	15
56209−0390	6.99 ± 0.77	0.07 ± 0.06	8.57 ± 0.97	–	–	2.86 ± 0.58	2.75 ± 0.55	0.39 ± 0.15	0.22 ± 0.14	0.52 ± 0.65	15
56298−0302	10.16 ± 1.84	0.09 ± 0.07	5.39 ± 0.46	–	–	2.86 ± 0.42	3.29 ± 0.49	1.59 ± 0.27	1.40 ± 0.24	7.00 ± 2.26	15
56366−0928	4.81 ± 0.41	0.12 ± 0.05	5.70 ± 0.40	–	0.21 ± 0.08	2.86 ± 0.28	2.51 ± 0.25	0.96 ± 0.12	0.96 ± 0.12	2.31 ± 0.56	15
55742−0383	2.74 ± 0.55	0.05 ± 0.01	4.99 ± 0.10	0.049 ± 0.038	–	2.86 ± 0.08	2.06 ± 0.06	0.63 ± 0.03	0.56 ± 0.03	1.01 ± 0.14	15
55302−0655	4.90 ± 0.18	0.05 ± 0.02	2.06 ± 0.05	0.035 ± 0.019	–	2.86 ± 0.08	1.67 ± 0.06	1.24 ± 0.04	1.00 ± 0.04	0.94 ± 0.14	15
56328−0550	6.45 ± 0.26	0.06 ± 0.02	4.90 ± 0.15	–	0.06 ± 0.04	2.86 ± 0.13	3.35 ± 0.16	1.10 ± 0.06	0.86 ± 0.06	1.57 ± 0.25	15
55646−0770	8.48 ± 2.32	0.14 ± 0.05	7.32 ± 1.31	–	–	2.86 ± 0.95	3.74 ± 1.23	1.50 ± 0.56	1.39 ± 0.52	1.82 ± 1.49	15
55617−0758	8.05 ± 0.33	0.05 ± 0.04	3.84 ± 0.20	–	0.11 ± 0.06	2.86 ± 0.27	2.26 ± 0.22	1.24 ± 0.14	1.38 ± 0.15	1.33 ± 0.40	15
56003−0218	3.35 ± 1.00	0.07 ± 0.04	4.70 ± 0.29	–	0.10 ± 0.07	2.86 ± 0.22	1.68 ± 0.15	0.56 ± 0.09	0.58 ± 0.09	2.06 ± 0.45	15
55629−0364	9.11 ± 0.64	0.11 ± 0.07	7.08 ± 0.52	0.031 ± 0.021	–	2.86 ± 0.41	3.91 ± 0.57	1.44 ± 0.24	1.32 ± 0.23	1.64 ± 0.80	15
56568−0076	5.12 ± 0.59	0.03 ± 0.01	3.16 ± 0.05	–	–	2.86 ± 0.09	2.98 ± 0.10	0.71 ± 0.03	0.69 ± 0.03	0.66 ± 0.09	15
55836−0160	3.57 ± 0.33	0.04 ± 0.02	3.70 ± 0.11	–	–	2.86 ± 0.14	2.24 ± 0.11	0.67 ± 0.05	0.59 ± 0.05	1.71 ± 0.32	15
55505−0654	3.05 ± 0.19	0.04 ± 0.02	7.95 ± 0.28	–	0.05 ± 0.03	2.86 ± 0.17	2.70 ± 0.16	0.65 ± 0.05	0.58 ± 0.05	2.10 ± 0.35	15

Note. References: 1 – Dopita et al. (2015); 2 – Bergvall, Johansson & Olofsson (1986); 3 – Phillips, Charles & Baldwin (1983); 4 – Koski (1978); 5 – Kraemer et al. (1994); 6 – Shuder (1980); 7 – Thomas et al. (2017); 8 – Cohen (1983); 9 – Goodrich & Osterbrock (1983); 10 – Malkan & Oke (1983); 11 – Alloin et al. (1992); 12 – Riffel et al. (2006); 13 – Rodríguez-Ardila et al. (2011); 14 – Ramos Almeida et al. (2006); and 15 – BOSS/SDSS sample. [a]Reference that the [S III]λ9069 emission-line fluxes was compiled. [b]Emission-line intensities corrected by reddening in this work. [c]Object that the [S III]λ9069 was measured with the others.

Table A2. Electron density and electron temperature values assumed in the ionic abundance calculations. $T_e(O^{2+})$ was calculated through the observational RO3 line ratio, whose line intensities are listed in Table A1, and by using the PYNEB code (Luridiana et al. 2015). $T_e(N^+)$ and $T_e(S^{2+})$ were calculated either from RN2 and RS3 line ratios (when these line ratios were measured), respectively, or from equations (3) and (4) (when auroral lines were not measured, see Table A1).

Object	$T_e(O^{2+})$ (K)	$T_e(S^{2+})$ (K)	$T_e(N^+)$ (K)	N_e (cm^{-3})
Mrk 573	12 888 ± 425	21 341 ± 7881	11 673 ± 1899	559 ± 102
NGC 5728	12 301 ± 725	20 030 ± 7929	11 373 ± 1923	674 ± 167
ESO 428 G14	15 651 ± 1197	27 501 ± 8055	13 082 ± 1983	1059 ± 466
NGC 4388	13 446 ± 1254	22 585 ± 8074	11 958 ± 1992	393:
Mrk 78	12 162 ± 1139	19 721 ± 8036	11 303 ± 1974	475:
NGC 7674	11 296 ± 1126	17 790 ± 8032	10 861 ± 1972	1396 ± 620
NGC 2110	20 761 ± 3395	38 896 ± 9338	15 688 ± 2561	691 ± 300
NGC 7682	14 146 ± 1412	24 146 ± 8131	12 315 ± 2020	1067 ± 495
NGC 3227	25 028 ± 2500	48 412 ± 17000	17 864 ± 5800	1067 ± 485
Mrk 1066	15 446 ± 3553	27 045 ± 9466	12 978 ± 2616	1122:
Mrk 3	15 335 ± 1185	26 796 ± 8051	12 921 ± 1981	500:
ESO 138 G1	21 996 ± 1318	41 650 ± 8097	16 318 ± 2003	1039 ± 452
55978−0990	12 685 ± 2490	20 888 ± 8684	11 570 ± 2274	266:
56104−0966	10 754 ± 1095	16 582 ± 8023	10 585 ± 1968	471 ± 210
55181−0154	10 508 ± 1855	24 392 ± 9679	10 459 ± 2111	778 ± 384
56088−0473	10 566 ± 301	9244 ± 1351	10 488 ± 1893	502 ± 186
56034−0154	12 184 ± 409	11 052 ± 2481	11 314 ± 1898	537 ± 167
56067−0382	16 612 ± 5030	29 644 ± 10845	31 422 ± 9900	666:
56240−0340	15 912 ± 3588	28 083 ± 9495	13 215 ± 2628	200:
55539−0167	12 334 ± 1976	20 105 ± 8387	16 670 ± 5500	445 ± 218
56626−0636	11 409 ± 726	27 152 ± 5997	10 919 ± 1923	537 ± 137
56074−0045	11 954 ± 1531	19 258 ± 8179	11 197 ± 2042	127 ± 58
55212−0380	10 644 ± 1185	16 335 ± 8051	10 528 ± 1981	699 ± 315
56399−0302	17 311 ± 5347	31 203 ± 11175	13 929 ± 3316	50:
56001−0293	11 159 ± 640	17 484 ± 7913	13 152 ± 4500	55:
55651−0052	9576 ± 733	18 122 ± 2797	9984 ± 1923	555 ± 130
56566−0794	11 713 ± 1806	21 676 ± 7539	10 771 ± 3800	347 ± 162
56748−0336	11 981 ± 3128	19 319 ± 9129	11 211 ± 2471	477:
56206−0454	12 842 ± 1266	16 315 ± 7012	11 649 ± 1994	266 ± 130
55860−0112	13 038 ± 3931	27 975 ± 12880	11 749 ± 2753	735 ± 360
56453−0144	11 224 ± 1400	17 630 ± 8127	10 824 ± 2017	410 ± 202
55710−0116	11 189 ± 1218	10 917 ± 2756	10 806 ± 1986	1021 ± 381
56209−0390	10 735 ± 3862	16 538 ± 8150	10 575 ± 2728	198 ± 49
56298−0302	14 006 ± 5604	23 833 ± 11451	12 243 ± 3425	451 ± 215
56366−0928	15 523 ± 3682	30 648 ± 9727	13 017 ± 2662	839 ± 410
55742−0383	11 497 ± 889	18 239 ± 7966	12 245 ± 3500	445 ± 206
55302−0655	16 672 ± 3674	29 778 ± 9568	11 547 ± 3178	267 ± 122
56328−0550	12 373 ± 1714	14 346 ± 5621	11 410 ± 2080	192:
55646−0770	14 856 ± 3805	25 729 ± 9680	12 676 ± 2706	593:
55617−0758	12 640 ± 4540	27 347 ± 10109	11 546 ± 2987	1168 ± 560
56003−0218	13 337 ± 3563	16 884 ± 8330	11 902 ± 2620	913 ± 430
55629−0364	13 575 ± 4192	22 872 ± 10028	12 023 ± 2852	546:
56568−0076	11 281 ± 1368	17 756 ± 8115	10 853 ± 2012	666 ± 215
55836−0160	11 814 ± 2314	18 946 ± 8576	11 125 ± 2225	427 ± 205
55505−0654	9268 ± 1446	11 052 ± 2955	9827 ± 2026	422 ± 190

Note. For some objects we use ':' to indicate that error bars are at least an order of magnitude larger than the expected density. This is due to the significant emission-line errors (see Section 3.1).

Table A3. Ionic and total abundances for Seyfert 2 nuclei derived through the T_e method.

Object	O^+/H^+	O^{2+}/H^+	O/H	S^+/H^+	S^{2+}/H^+	ICF(S)	S/H	S/O
Mrk 573	7.95 ± 0.12	8.21 ± 0.04	8.58 ± 0.13	6.46 ± 0.12	6.52 ± 0.16	2.02	7.08 ± 0.18	-1.50 ± 0.22
NGC 5728	8.03 ± 0.12	8.22 ± 0.07	8.61 ± 0.14	6.52 ± 0.12	6.42 ± 0.17	1.81	7.07 ± 0.18	-1.55 ± 0.23
ESO 428 G14	7.79 ± 0.10	8.03 ± 0.07	8.40 ± 0.12	6.44 ± 0.10	6.24 ± 0.15	1.95	6.94 ± 0.16	-1.46 ± 0.20
NGC 4388	8.03 ± 0.12	8.17 ± 0.09	8.59 ± 0.13	6.37 ± 0.12	6.12 ± 0.16	1.83	6.85 ± 0.18	-1.74 ± 0.22
Mrk 78	8.38 ± 0.13	8.35 ± 0.10	8.84 ± 0.14	6.41 ± 0.13	6.10 ± 0.17	1.52	6.87 ± 0.19	-1.97 ± 0.23
NGC 7674	7.85 ± 0.13	8.47 ± 0.10	8.74 ± 0.15	6.47 ± 0.13	6.71 ± 0.18	2.94	7.20 ± 0.19	-1.54 ± 0.24
NGC 2110	7.84 ± 0.10	7.39 ± 0.09	8.15 ± 0.11	6.50 ± 0.10	6.30 ± 0.14	1.22	6.71 ± 0.16	-1.43 ± 0.19
NGC 7682	7.99 ± 0.12	8.06 ± 0.09	8.50 ± 0.13	6.61 ± 0.11	6.33 ± 0.16	1.61	7.08 ± 0.17	-1.42 ± 0.22
NGC 3227	7.55 ± 0.14	7.59 ± 0.06	8.04 ± 0.15	6.36 ± 0.15	6.28 ± 0.19	1.72	6.62 ± 0.21	-1.42 ± 0.26
Mrk 1066	7.98 ± 0.13	7.58 ± 0.11	8.30 ± 0.14	6.24 ± 0.13	5.85 ± 0.17	1.21	6.68 ± 0.19	-1.62 ± 0.24
Mrk 3	8.16 ± 0.11	8.05 ± 0.07	8.58 ± 0.12	6.62 ± 0.11	6.40 ± 0.15	1.46	7.11 ± 0.17	-1.47 ± 0.21
ESO 138 G1	7.52 ± 0.08	7.60 ± 0.05	8.04 ± 0.09	6.00 ± 0.08	5.78 ± 0.12	1.74	6.20 ± 0.14	-1.83 ± 0.16
55978−0990	8.49 ± 0.14	8.25 ± 0.09	8.86 ± 0.15	6.55 ± 0.14	6.43 ± 0.18	1.35	7.09 ± 0.20	-1.78 ± 0.25
56104−0966	8.60 ± 0.14	8.37 ± 0.11	8.97 ± 0.15	6.44 ± 0.14	6.12 ± 0.18	1.32	6.90 ± 0.20	-2.08 ± 0.25
55181−0154	8.42 ± 0.15	8.36 ± 0.11	8.87 ± 0.16	6.48 ± 0.15	6.34 ± 0.19	1.43	7.01 ± 0.21	-1.86 ± 0.26
56088−0473	8.13 ± 0.14	8.35 ± 0.04	8.73 ± 0.15	5.74 ± 0.14	6.50 ± 0.18	1.89	6.86 ± 0.20	-1.87 ± 0.25
56034−0154	8.16 ± 0.12	8.35 ± 0.04	8.74 ± 0.14	6.53 ± 0.12	6.87 ± 0.17	1.87	7.32 ± 0.18	-1.41 ± 0.23
56067−0382	7.58 ± 0.16	7.86 ± 0.13	8.04 ± 0.17	6.03 ± 0.15	6.01 ± 0.19	1.31	6.32 ± 0.21	-1.72 ± 0.27
56240−0340	8.38 ± 0.13	7.82 ± 0.10	8.66 ± 0.14	6.43 ± 0.13	6.44 ± 0.17	1.18	7.03 ± 0.19	-1.63 ± 0.23
55539−0167	7.58 ± 0.15	7.87 ± 0.10	8.22 ± 0.16	6.03 ± 0.15	6.17 ± 0.20	1.32	6.70 ± 0.22	-1.53 ± 0.27
56626−0636	8.32 ± 0.13	8.14 ± 0.07	8.72 ± 0.14	6.65 ± 0.13	6.06 ± 0.17	1.35	7.04 ± 0.19	-1.68 ± 0.24
56074−0045	8.35 ± 0.13	7.73 ± 0.09	8.62 ± 0.14	6.41 ± 0.13	6.12 ± 0.17	1.15	6.88 ± 0.19	-1.74 ± 0.24
55212−0380	8.34 ± 0.14	8.55 ± 0.10	8.94 ± 0.15	6.62 ± 0.14	6.65 ± 0.18	1.81	7.22 ± 0.20	-1.71 ± 0.25
56399−0302	8.10 ± 0.14	7.37 ± 0.12	8.35 ± 0.15	6.51 ± 0.14	6.47 ± 0.18	1.13	6.79 ± 0.20	-1.56 ± 0.25
56001−0293	8.19 ± 0.17	8.27 ± 0.07	8.71 ± 0.18	6.29 ± 0.15	6.41 ± 0.19	1.38	6.95 ± 0.21	-1.76 ± 0.28
55651−0052	8.41 ± 0.15	8.16 ± 0.10	8.78 ± 0.16	6.58 ± 0.15	6.17 ± 0.19	1.28	7.01 ± 0.21	-1.77 ± 0.26
56566−0794	8.57 ± 0.13	8.00 ± 0.11	8.85 ± 0.14	7.06 ± 0.16	6.18 ± 0.20	1.16	7.40 ± 0.22	-1.45 ± 0.26
56748−0336	8.39 ± 0.15	8.14 ± 0.12	8.76 ± 0.16	6.58 ± 0.15	6.43 ± 0.19	1.32	7.10 ± 0.21	-1.66 ± 0.26
56206−0454	8.51 ± 0.12	8.03 ± 0.10	8.81 ± 0.14	6.56 ± 0.12	6.30 ± 0.17	1.20	7.04 ± 0.18	-1.77 ± 0.23
55860−0112	8.37 ± 0.15	8.08 ± 0.12	8.72 ± 0.16	6.83 ± 0.15	6.21 ± 0.19	1.27	7.22 ± 0.21	-1.51 ± 0.27
56453−0144	8.26 ± 0.14	8.19 ± 0.09	8.70 ± 0.15	6.56 ± 0.14	6.56 ± 0.18	1.47	7.15 ± 0.20	-1.55 ± 0.25
55710−0116	8.18 ± 0.13	8.26 ± 0.11	8.70 ± 0.15	6.72 ± 0.13	6.97 ± 0.18	1.58	7.45 ± 0.20	-1.25 ± 0.24
56209−0390	8.66 ± 0.17	8.38 ± 0.13	9.02 ± 0.18	6.12 ± 0.14	5.97 ± 0.19	1.32	6.65 ± 0.20	-2.37 ± 0.27
56298−0302	8.56 ± 0.16	7.83 ± 0.13	8.81 ± 0.17	6.70 ± 0.15	6.89 ± 0.19	1.10	7.40 ± 0.21	-1.42 ± 0.27
56366−0928	8.13 ± 0.13	7.74 ± 0.11	8.46 ± 0.14	6.48 ± 0.13	6.81 ± 0.17	1.22	6.98 ± 0.19	-1.48 ± 0.24
55742−0383	7.99 ± 0.16	8.04 ± 0.09	8.50 ± 0.17	6.30 ± 0.15	6.20 ± 0.20	1.41	6.84 ± 0.21	-1.65 ± 0.28
55302−0655	8.35 ± 0.16	7.23 ± 0.11	8.56 ± 0.18	6.61 ± 0.15	5.91 ± 0.20	1.09	6.98 ± 0.21	-1.58 ± 0.28
56328−0550	8.50 ± 0.13	7.94 ± 0.11	8.78 ± 0.14	6.56 ± 0.13	6.55 ± 0.17	1.17	7.15 ± 0.19	-1.63 ± 0.24
55646−0770	8.42 ± 0.13	7.90 ± 0.11	8.71 ± 0.15	6.66 ± 0.14	6.26 ± 0.18	1.17	7.10 ± 0.20	-1.62 ± 0.25
55617−0758	8.54 ± 0.16	7.81 ± 0.12	8.79 ± 0.17	6.74 ± 0.16	6.10 ± 0.21	1.09	7.12 ± 0.22	-1.67 ± 0.28
56003−0218	8.11 ± 0.14	7.83 ± 0.11	8.47 ± 0.15	6.34 ± 0.14	6.56 ± 0.19	1.27	7.05 ± 0.20	-1.42 ± 0.26
55629−0364	8.54 ± 0.15	7.99 ± 0.12	8.82 ± 0.16	6.69 ± 0.15	6.28 ± 0.19	1.16	7.12 ± 0.21	-1.70 ± 0.26
56568−0076	8.45 ± 0.14	7.87 ± 0.10	8.73 ± 0.15	6.50 ± 0.13	6.03 ± 0.18	1.13	6.92 ± 0.20	-1.81 ± 0.25
55836−0160	8.26 ± 0.14	7.88 ± 0.11	8.59 ± 0.15	6.41 ± 0.14	6.41 ± 0.18	1.23	7.00 ± 0.20	-1.59 ± 0.25
55505−0654	8.42 ± 0.15	8.56 ± 0.11	8.97 ± 0.17	6.53 ± 0.16	6.87 ± 0.20	1.74	7.33 ± 0.22	-1.65 ± 0.27

This paper has been typeset from a TeX/LaTeX file prepared by the author.